Unravelling drug resistant proteotypes through phenotype-resolved proteomics of single-cell derived colonies

Di Qin[1,2], Ridhima Das[3], Simon Schallenberg[4], Kristoffer Riecken[5], Ingeborg Tinhofer[3,6], and Fabian Coscia[1*]

[1]Max-Delbrück-Center for Molecular Medicine in the Helmholtz Association (MDC), Spatial Proteomics Group, Berlin, Germany

[2]Charité - Universitätsmedizin Berlin, corporate member of Freie Universität Berlin and Humboldt Universität zu Berlin, Charitéplatz 1, 10117 Berlin, Germany

[3]Department of Radiooncology and Radiotherapy, Translational Radiation Oncology Research Laboratory, Charité - Universitätsmedizin Berlin, corporate member of Freie Universität Berlin and Humboldt Universität zu Berlin, Charitéplatz 1, 10117 Berlin, Germany

[4]Institute of Pathology, Charité-Universitätsmedizin Berlin, Corporate Member of Freie Universität Berlin, Humboldt-Universität zu Berlin and Berlin Institute of Health, Berlin, Germany

[5]Research Department Cell and Gene Therapy, Department of Stem Cell Transplantation, University Medical Center Hamburg-Eppendorf, Hamburg, Germany.

[6]German Cancer Research Center (DKFZ), Heidelberg, and German Cancer Consortium (DKTK), partner site Berlin, Germany

[*]For correspondence: fabian.coscia@mdc-berlin.de

Keywords: Proteomics, drug resistance, microscopy, tumor heterogeneity

Summary

Drug resistance in cancer therapy continues to significantly contribute to treatment failure and disease progression, and is linked to intratumoral heterogeneity. Mass spectrometry (MS)-based single-cell proteomics (SCP) provides a unique opportunity to uncover the mechanisms underlying drug-resistant phenotypes; however, current methods lack clonal resolution and are often confounded by cell cycle and cell size differences. Here, we introduce PhenoSCoP, a microscopy-guided discovery proteomics concept for mapping clonal proteomic heterogeneity. By distinguishing between transient and long-lived protein level changes, our approach uncovered hereditary and clone-specific programs associated with chemotherapeutic responses in head and neck squamous cell carcinoma (HNSCC) cells. Combined with fluorescence barcoding and drug treatment assays, we identified pre-existing proteotypes that strongly dominated drug-resistant cell populations. These programs also emerged in HNSCC patient samples and in relapsed tumors after chemoradiotherapy, linking drug-resistant proteotypes to intra- and inter-tissue spatial heterogeneity. In summary, we describe a robust, versatile and phenotype-resolved approach for uncovering single-cell-derived proteotypes associated with the therapeutic responses of distinct tumor cell clones.

Introduction

Resistance to anti-cancer therapies, including targeted, chemo, and immunotherapies, remains a major obstacle for successful treatment outcomes [1]. While extensive research has focused on the genetic mechanisms of drug resistance and tumor heterogeneity [2,3], non-genetic mechanisms that confer transient or permanent resistance are increasingly being recognized as important drivers of therapeutic responses [4]. Cancer cells exploit both genetic and non-genetic drug resistance programs, emphasizing the importance of methodologies that capture both mechanisms on a global, phenotype-centric and quantitative scale [5]. Studying the global proteome of distinct tumor cell clones, a close proxy for cellular function [6], is therefore of paramount importance to unravel the mechanisms underlying differential treatment responses and for identifying clone-specific vulnerabilities.

A growing body of literature supports the notion that cellular states before drug treatment dictate treatment outcomes [7–9], including observations from clinical samples [10,11]. Identifying such pre-existing molecular programs associated with clone-specific survival is hence of high clinical value for discovering novel therapeutic strategies and for eradicating the most aggressive and resistant clones within heterogeneous tumors. However, the extent to which clonal proteomic heterogeneity and pre-existing proteotypes drive therapeutic outcomes and drug resistance remains poorly understood. Based on imaging-based proteomics, it has been estimated that one-fifth of the human proteome exhibits cell-to-cell variability [12], emphasizing the importance of single-cell analyses in the context of treatment responses. High-content imaging offers great insights into the proteome at subcellular and spatiotemporal resolutions, yet only a few proteins can be profiled simultaneously [13–16]. A promising and emerging methodology to study drug-resistant proteotypes is single-cell proteomics (SCP) by mass spectrometry, which currently achieves a depth of a few thousand proteins [17–21]. However, compared to bulk based profiling, SCP poses considerable challenges for data interpretation, for example due to data sparsity and confounding factors from cell size and cell cycle differences [22–24]. This emphasizes the importance of hybrid methods that combine the complementary strengths of bulk and SCP to capture single-cell-derived proteotypes on a global and quantitative scale.

To bridge this gap, we propose PhenoSCoP, a discovery proteomics concept that combines fluorescence microscopy, laser microdissection (LMD), and ultrasensitive MS-based proteomics. Instead of analyzing true single cells, we developed a scalable workflow to profile single-cell-derived colonies without extensive serial dilution and clonal expansion experiments. Inspired by elegant work conducted on transcriptional memory, spanning time frames of several cell cycles [9] to weeks [8] and even years [25], we hypothesized that single-cell clones maintain distinct and quantifiable proteomic traits that underlie stable drug-resistant phenotypes. The concept of protein level memory and its implications in driving cellular function have been demonstrated previously [26,27], however, the extent to which the cellular proteome features clone-specific, heritable, and phenotype-dictating traits remains largely unexplored. Our approach offers an easy-to-implement solution to prioritize heritable protein level changes while mitigating short-lived and transient fluctuations that often confound SCP experiments. By applying PhenoSCoP to head and neck cancer cell lines, we demonstrated the unique ability of our method to identify rare, pre-resistant proteotypes from drug-naïve populations. Combined with spatial proteomics of primary and recurrent tumor samples, we demonstrated the relevance of the prioritized proteins in specimens from patients with head and neck cancer.

Results

An optimized workflow for immunofluorescence microscopy guided discovery proteomics

Our goal was to develop an imaging-guided discovery proteomics method that captures clone-specific proteotypes functionally linked to differential drug responses (**Fig. 1A**). We devised **Pheno**type-resolved **S**ingle-**Co**lony **P**roteomics (PhenoSCoP), which combines clonogenic cell growth, fluorescence microscopy, laser microdissection (LMD) and ultrasensitive mass spectrometry (MS)-based proteomics. Our method was inspired by the clonogenic survival assay first described in 1956 by Puck and Marcus [28]. This assay is a gold standard for evaluating cellular viability and measuring the proportion of surviving reproductive cells following treatment, thereby enabling the investigation of long-term cellular outcomes [29]. Instead of analyzing single cells, we sought to analyze single-cell-derived phenotypes. Cells are seeded on microscopy slides at low concentrations, exposed to drug treatment, and outgrowth into multicellular colonies is monitored, visualized and quantified. Finally, drug-tolerant and colony-forming cells are isolated and quantitatively compared to untreated controls using MS-based proteomics.

To realize PhenoSCoP, we first optimized the staining and imaging workflow and assessed the impact of fixation and permeabilization on the quantitative proteomic read-out. FaDu cells, an established polyclonal model for studying CP resistance in head and neck squamous cell carcinoma (HNSCC) [30], were seeded on polyphenylene sulfide (PPS) metal frame slides required for laser microdissection, grown to ~ 80% confluence, and subjected to different protocols prior to LMD and MS-based proteomics (**Fig. 1B**). The comparison of fresh FaDu cells with formaldehyde-fixed cells (4%, 10 min) resulted in almost identical proteome coverage, in line with a recent study [31]. From the small 100-cell regions, we quantified more than 6,000 unique proteins in a 15-min active liquid chromatography (LC) gradient on a Bruker timsTOF Ultra instrument operated in diaPASEF mode [32] and based on library-free DIA-NN [33] analysis (**Fig. 1B**). To enable the staining of intracellular proteins critical for image-based cell phenotyping, we tested two standard permeabilization protocols based on 90% ice-cold methanol or 0.2% Triton X-100. While both protocols resulted in slightly lower proteome coverage than fixation alone (< 4%), quantitatively, the methanol protocol performed better and was closer to the fixation-only condition than Triton X-100 treated cells (**Fig. 1C, Suppl. Fig. 1B**), in agreement with previous work [34]. Importantly,

despite the lower number of identified proteins after permeabilization, global proteomic inter-group correlations were still excellent (median Pearson r = 0.97, **Fig. 1D**). Therefore, formaldehyde fixation combined with methanol permeabilization was selected as our final protocol. Next, we seeded FaDu cells onto PPS metal frame slides and monitored colony formation over ten days of growth. At day ten, cells were formaldehyde-fixed and subjected to whole-slide immunofluorescence imaging (**Fig. 1E**). We validated the high staining and imaging quality using primary conjugated antibodies targeting cytoplasmic pan-cytokeratin (panCK) and the S-phase marker Ki-67, as well as EdU (replicating cells) and DAPI (DNA) staining (**Fig. 1E**). Following imaging, we isolated distinct colonies by laser microdissection, providing sufficient cellular input for deep and robust proteome profiling (**Fig. 1F**).

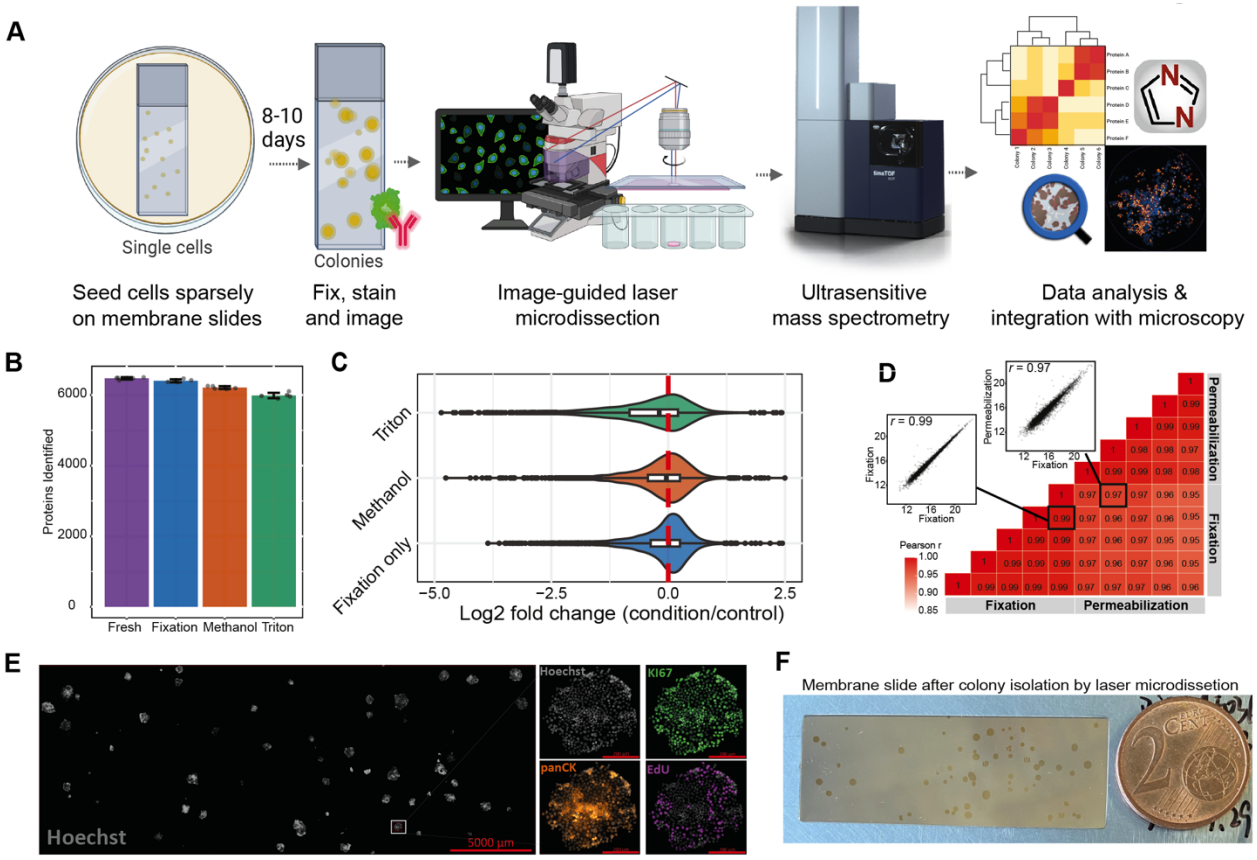

Fig. 1 Phenotype-resolved Single-Colony Proteomics (PhenoSCoP) workflow optimization.
(A) Schematic representation of the PhenoSCoP approach. **(B)** Comparison of protein identifications from approximately 100 laser microdissected cells prepared using four different protocols: fresh cells, formaldehyde (FA) fixed cells, FA fixed cells permeabilized using ice-cold methanol and Triton-X-100. **(C)** Quantitative proteomic comparison of fixation-only and permeabilized cells relative to untreated (fresh) control cells. Only common proteins were used without data imputation. **(D)** Sample Pearson correlation matrix of all replicates for fixation-only and methanol-permeabilized cells. **(E)** Whole-slide immunofluorescence imaging of colonies grown on a PPS membrane slide using the optimized staining protocol. One representative colony corresponding to the white box is shown in the

right panel, highlighting nuclear and cytosolic staining. Hoechst (grey), Ki-67 (green), Pan-CK (orange) and EdU stained S-phase cells (pink). Scale bar for the overview image (left panel) is 5,000 µm, and 200 µm for example colonies (right panel). **(F)** Image of the PPS slide after colony isolation using laser microdissection.

PhenoSCoP effectively captures clonal differences while mitigating SCP confounders

We aimed to develop a method that captures and quantifies single-cell-derived phenotypes while minimizing SCP confounders, such as cell cycle and cell size differences [23] (**Fig. 2A).** Working with clonal averages instead of single cells has several advantages for studying the mechanisms underlying treatment resistance. Protein level variations from transient fluctuations (e.g., cell cycle regulation) are averaged out, whereas heritable, long-lasting (i.e., propagated to several daughter generations), and clone-specific molecular programs are preserved and reflected in the quantitative proteomic read-out.

To test whether our approach effectively captured clone-specific proteotypes (**Fig. 2A**), we applied PhenoSCoP to the polyclonal HNSCC model FaDu. We isolated and profiled 36 colonies as well as and 10 mini-bulk samples acting as controls samples. Mini-bulk samples consisted of homogenous and non-sparsely seeded cells that failed to grow into individual colonies but were otherwise cultivated under identical growth conditions (**Fig. 2B**). All samples were processed and measured within the same experimental batch. On average, we consistently quantified 6,208 proteins per colony with high data completeness across samples, which was, as expected, much superior to single-cell proteomic measurements of the same cells (**Suppl. Fig. 2A-B**). This allowed us to successfully capture biological differences between individual colonies, as proteomic variation from different colonies significantly exceeded that of our mini-bulk measurements (median CV 20% *vs.* 14%, $p < 2.2e-16$) (**Fig. 2B**). In support of this, the proteomes of cells isolated from the same colony were quantitatively more similar than those of cells from neighbouring colonies (Pearson $r = 0.98$ *vs.* 0.95, respectively, **Fig. 2C**). Together, these results showed that our approach captured hereditary proteomic traits shared between cells of the same (sub)clonal origin.

Next, we reasoned that our precise protein quantification strategy in combination with clonal average measurements would additionally allow us to distinguish different biological sources of protein-level variability. As expected, rapidly and transiently fluctuating proteins (i.e., within one cell cycle), such as cell cycle-regulated proteins, showed little variation across colonies (**Fig. 2D;** for example, MCM proteins). Similarly, proteins involved in reported 'housekeeping' functions

(e.g., GAPDH, ATP1A1, and PGK1) showed stable protein levels across colonies (**Fig. 2D-E**). Notably, we identified dozens of proteins that showed significant differences in abundance among single-cell-derived colonies, including the metastasis-associated protein DPYSL3 [35], interferon-response protein DDX60, and heat shock protein beta-1 (HSPB1) (**Fig. 2D-E**). Overall, we found an inverse correlation between protein level variability and protein essentiality, as revealed by the integration of cancer dependency map data (DepMap) [36] (**Fig. 2F**). In other words, the most variable proteins were less likely to be essential, whereas cell cycle regulators and 'housekeeper' proteins generally showed low variation, but high dependency scores (below 0). Immunofluorescence microscopy confirmed the different protein level patterns revealed by PhenoSCoP. For example, while DDX60 showed variable and clone-specific expression (**Fig. 2E**), ATP1A1 (Na/K ATPase) staining was positive for the majority of cells independent of the colony. Globally, the most variable and non-essential proteins were strongly enriched for cancer and immune-related pathways, such as the interferon response, KRAS signalling, and epithelial-to-mesenchymal transition (**Fig. 2F**)

Our quantitative proteomics data suggested that the overall cell cycle profile was comparable across colonies, as estimated by the quantification of S-phase-specific proteins, such as the minichromosome maintenance (MCM) protein family (**Fig. 2D**), essential for genomic DNA replication. Integrating EdU staining coupled with machine-learning-based image analysis showed that for most colonies, approximately half of all cells (on average 47% ± 11%) were in early or late S-phase (**Fig. 2H-I**). Interestingly, our microscopy-guided approach also enabled us to identify rare outlier phenotypes that deviated from this cell line average. For example, one colony mostly featured slow-cycling cells, with only 25% of EdU+ cells, whereas two colonies were highly proliferative, with over 70% EdU+ cells (**Fig. 2H**). Our matching proteomics data of such colonies confirmed significantly higher MCM protein levels (e.g., MCM4 and MCM5) when we compared the least and most proliferative phenotypes (**Fig. 2I**). Importantly, we observed no difference in proteome coverage, despite the expected differences in the total number of cells per colony (**Fig. 2I**). Hence, our approach provides a robust and balanced solution to capture clone-specific and rare cellular phenotypes while mitigating cell size and cell cycle differences that often confound single-cell proteomics data.

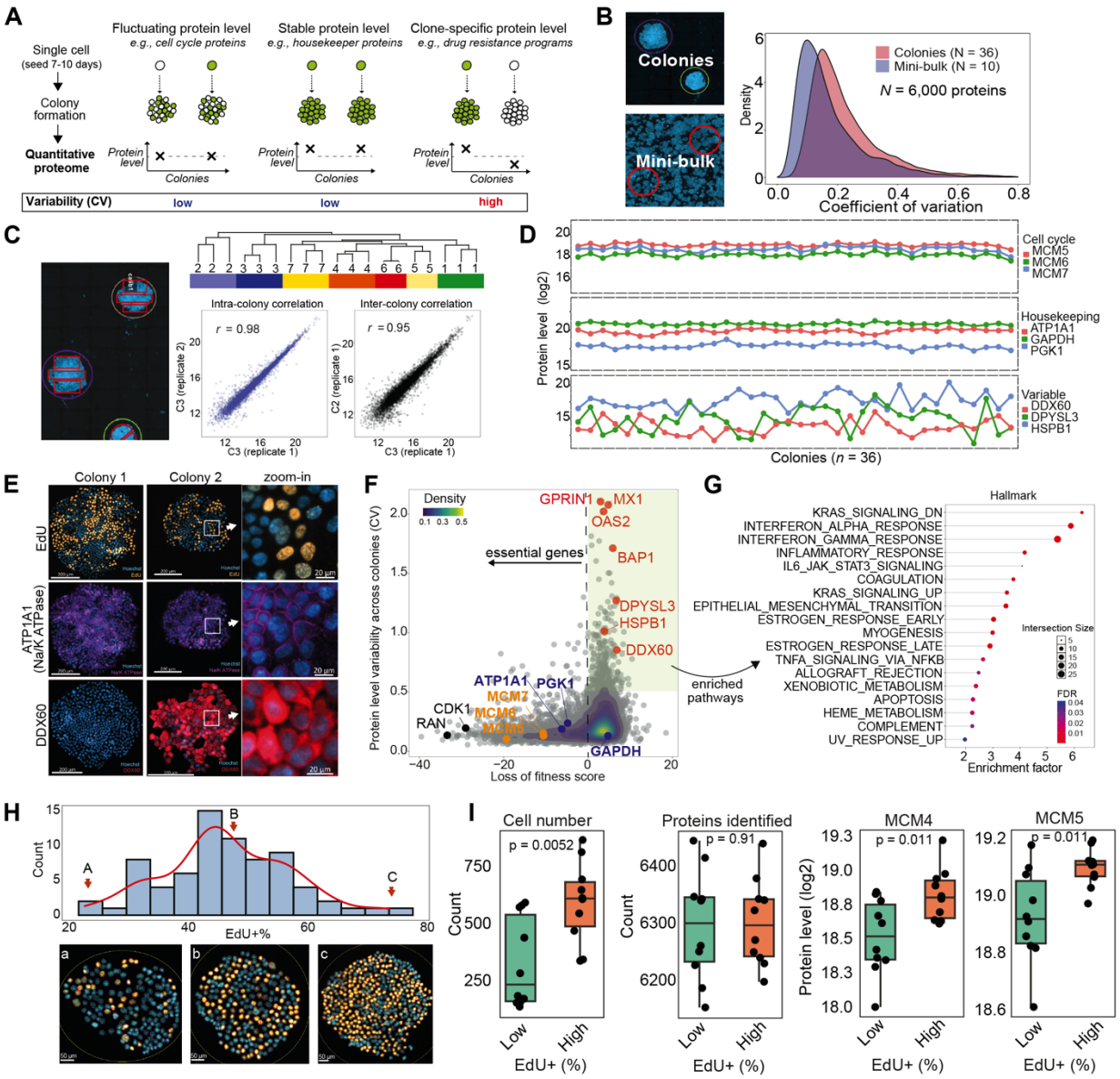

Fig. 2 PhenoSCoP captures clone-specific proteomic signatures while mitigating SCP confounders.
(A) Schematic scenarios of protein level variation in single-cell-derived colonies. Fluctuating, stable, and hereditary protein level changes are distinguished from quantitative proteome measurements. **(B)** Left: Example images of Hoechst-stained colonies and homogenously grown cells (mini-bulk). Right: Density plot showing the coefficient of variation (CV) of protein quantification from single-cell-derived colonies (n = 36) and mini-bulk replicates (n = 10). **(C)** Intra-colony proteomic comparison. Seven colonies were separated into two to three replicates using laser microdissection and subjected to proteome analysis. Unsupervised hierarchical clustering based on 6,088 quantified proteins. Sample correlations between segments from the same colony (intra-colony) and different colonies (inter-colony) are shown. **(D)** Relative protein levels of 36 colonies illustrating the three scenarios shown in panel A. Upper panel: S-phase proteins (MCM5-7) represent cell cycle-dependent proteins. Note that fluctuating protein levels were averaged out in the colony proteomes. Middle panel: Stable housekeeping proteins (ATP1A1, GAPDH, and PGK1). Lower panel: Variable proteins between different colonies (DDX60, DPYSL3, and HSPB1). **(E)** Immunofluorescent images of representative markers from different colonies, corresponding to the three protein types shown in panel D. Scale bar is 200 µm for colonies and 20 µm for the indicated regions. **(F)** Protein variability (coefficient of variation) *versus* gene essentiality (loss of fitness score in FaDu cells). Proteins from panel D are highlighted: yellow (cell cycle), blue (housekeeping), and red (variable proteins). Cell cycle and housekeeping proteins are essential proteins. **(G)**

Hallmark pathway enrichment of non-essential variable proteins from panel F. **(H)** Upper panel: Histogram showing the proportion of S-phase cells across 73 colonies determined by counting EdU-positive cells from IF image data. Lower panel: Representative images of colonies with low, medium, and high proportions of S-phase cells, corresponding to the upper panel. **(I)** Boxplots of cell counts, protein identifications, and MCM protein levels per colony for the top ten and bottom ten colonies shown in panel H. Student's *t*-test p values are indicated for each plot.

PhenoSCoP identifies molecular drivers of cisplatin resistance

Cisplatin (CP) is a cornerstone chemotherapy drug used to treat HNSCC, particularly in advanced stages; however, treatment failure due to primary and acquired resistance is common, particularly in human papilloma virus (HPV)-negative carcinomas [37]. High intratumoral heterogeneity and expansion of pre-resistant clones are the main drivers of cisplatin resistance in HNSCC [38–40]. The HPV-negative FaDu cell line is an established model for studying CP resistance in HNSCC and consists of multiple genetically and transcriptionally distinct subclones with varying CP sensitivities, differing by more than 100-fold [39]. In this cell line, Niehr *et al*. revealed a causal relationship between the p53 gain-of-function (GOF) missense mutation *TP53* p.R248L and increased CP resistance. Importantly, stabilizing *TP53* GOF mutations are associated with poor patient outcomes [41–43], emphasizing the need to better understand the molecular underpinnings and therapeutic vulnerabilities of such resistant clones. To test whether our method could identify pre-existing proteotypes associated with CP resistance, we employed a two-tiered strategy. First, we characterized two previously established single-cell-derived FaDu subclones with a known genetic background and CP sensitivity (**Fig. 3**). Second, we used an unbiased approach to determine whether chemotherapy resistance-associated proteotypes could be identified directly from treatment-naïve parental cells (**Fig. 4**).

We profiled the proteomes of two single-cell-derived and drug-naive clones representing stable CP-sensitive (C46 clone) and resistant (C5 clone) phenotypes, previously characterized by bulk-based genomics, transcriptomics, and phosphoproteomics (Niehr *et al*, 2018). Although both clones had an intronic *TP53* mutation (*TP53* c.673 G>A) resulting in an early stop codon, the CP-resistant C5 clone carried an additional *TP53*^{R248L} GOF mutation and an extra copy on chromosome 17 (encoding mutant p53). Additional mutations are summarized in **Suppl. Fig. 3A**. To confirm the stability of different levels of CP resistance, we combined PhenoSCoP with CP treatment. Cells from both clones were plated as single-cell dilutions on PPS membrane slides and treated for 24 h with their expected IC-50 CP concentrations (C46:30 ng/ml, C5:150 ng/ml).

Colony formation was then monitored over 10 days (**Fig. 3B**). On day 10, the colonies were fixed, stained, and subjected to whole-slide imaging and global proteomic analysis. CP treatment resulted in a reduction of approximately 50% in colony formation for both clones, confirming their respective IC-50 dosages. We isolated and profiled ~20 colonies of each clone and observed strong quantitative differences with 656 differentially abundant proteins (FDR < 0.05, **Fig. 3C-D, Suppl. Fig. 3B**). Consistent with our previous findings (**Fig. 2D**), non-significant proteins included 'housekeeping' proteins, such as GAPDH, ATP1A1, and PGK1, which showed little clonal variation. Notably, p53 was the most upregulated protein in CP-resistant clone 5 (**Fig. 3D**), confirming the strong protein stabilization effect of the R248L GOF mutation and its functional role as a driver of CP resistance. In the sensitive clone, p53 was undetectable at the baseline level (**Suppl. Fig. 3C**), in agreement with the destabilizing intronic mutation. Our exploratory proteomic data also shed light on the cellular mechanisms underlying p53 stabilization. We identified the chaperones HSP70 (HSP1A1) and HSP90 (HSP90AA1), which are critical mediators of mutant p53 stabilization and localization [44,45], among the top significantly regulated proteins (**Fig. 3C**). Previously reported amplification of chromosome 17 of the resistant clone was also strongly reflected in the quantitative proteome (**Suppl. Fig. 3D**). Interestingly, we uncovered an upregulation of chromosome 20 encoded proteins. Pathway enrichment analysis revealed upregulated DNA damage repair, ribosomal processes, and p53 signaling in the resistant clone, whereas the sensitive clone showed higher levels of proteins related to antigen presentation, interferon, and TNF signalling (**Suppl. Fig. 3D**). The strong and constitutive upregulation of DNA damage repair and DNA replication signatures in the resistant clone at baseline was intriguing, as it could explain one of the biological mechanisms behind the five-fold higher CP tolerance of this clone.

We next analyzed how these two genetically and proteomically distinct clones responded to CP treatment and whether drug-tolerant cells from both clones featured similar or diverging molecular programs. We found that drug tolerant cells that survived a single IC-50 dose of CP and formed reproductive colonies, featured similar protein and pathway-level changes (**Fig. 3E-G**). These included biological processes related to mitochondrial metabolism, DNA damage repair, proteasome degradation, and interferon response. While the genetically driven difference in p53 protein abundance remained stable between the two clones (**Fig. 3G**), proteins that showed similar changes after treatment included the complex I mitochondrial protein NDUFB11, the Fanconi

anemia ubiquitin ligase FANCL (a critical regulator of CP crosslink repair), ubiquitin conjugating enzyme UBE2D2, and interferon-stimulated ubiquitin-like protein ISG15. Notably, several enriched processes have been previously associated with non-genetic resistance programs and cancer cell plasticity. For example, constitutive type-I-interferon signaling has been identified as a non-genetic driver of primary drug resistance in several cancers [7,9,46,47].

We identified several proteins involved in mitochondrial metabolism and redox metabolism that were downregulated in drug-tolerant, colony-forming cells. NDUFB11, a complex I mitochondrial protein, was of particular interest, as it was the most downregulated protein after CP treatment in both clones (**Fig. 3E**). Reduced NDUFB11 protein levels have recently been linked to enhanced CP resistance in ovarian cancer models through increased protein degradation [48]. In agreement with Salovska *et al*, pathway enrichment analysis also showed an increase in the proteasome degradation machinery in drug-tolerant cells derived from both clones (**Fig. 3G**). To test whether NDUFB11 was indeed functionally relevant for CP tolerance in the FaDu model, we performed an NDUFB11 siRNA (3nM) knockdown experiment with and without CP. This resulted in a marked decrease in colony formation in the resistant C5 clone (-53%), whereas the polyclonal parental line was much less affected (-17%) (**Fig. 3H-I**). Notably, when combined with CP treatment, colony formation was nearly abolished in the resistant clone. The more detrimental effect on cell survival could be explained by the 2.5-fold lower NDUFB11 protein level at the baseline (**Fig. 3G**). Although NDUFB11 is a non-essential gene in most cancer cell lines, FaDu cells exhibit moderate dependency on NDUFB11, as shown by CRIPSR-based knock-out data (**Suppl. Fig. 3E**). Our data showed clone-specific effects of NDUFB11 knockdown and suggested that p53-mutant clones could be particularly sensitive to NDUFB11 deficiency. Further research is needed to determine whether targeting NDUFB11, or more globally mitochondrial redox metabolism, could be exploited therapeutically to eradicate p53-mutant HNSCC clones.

Collectively, these data demonstrate the potential and versatility of PhenoSCoP in uncovering the genetic and non-genetic drivers of drug resistance.

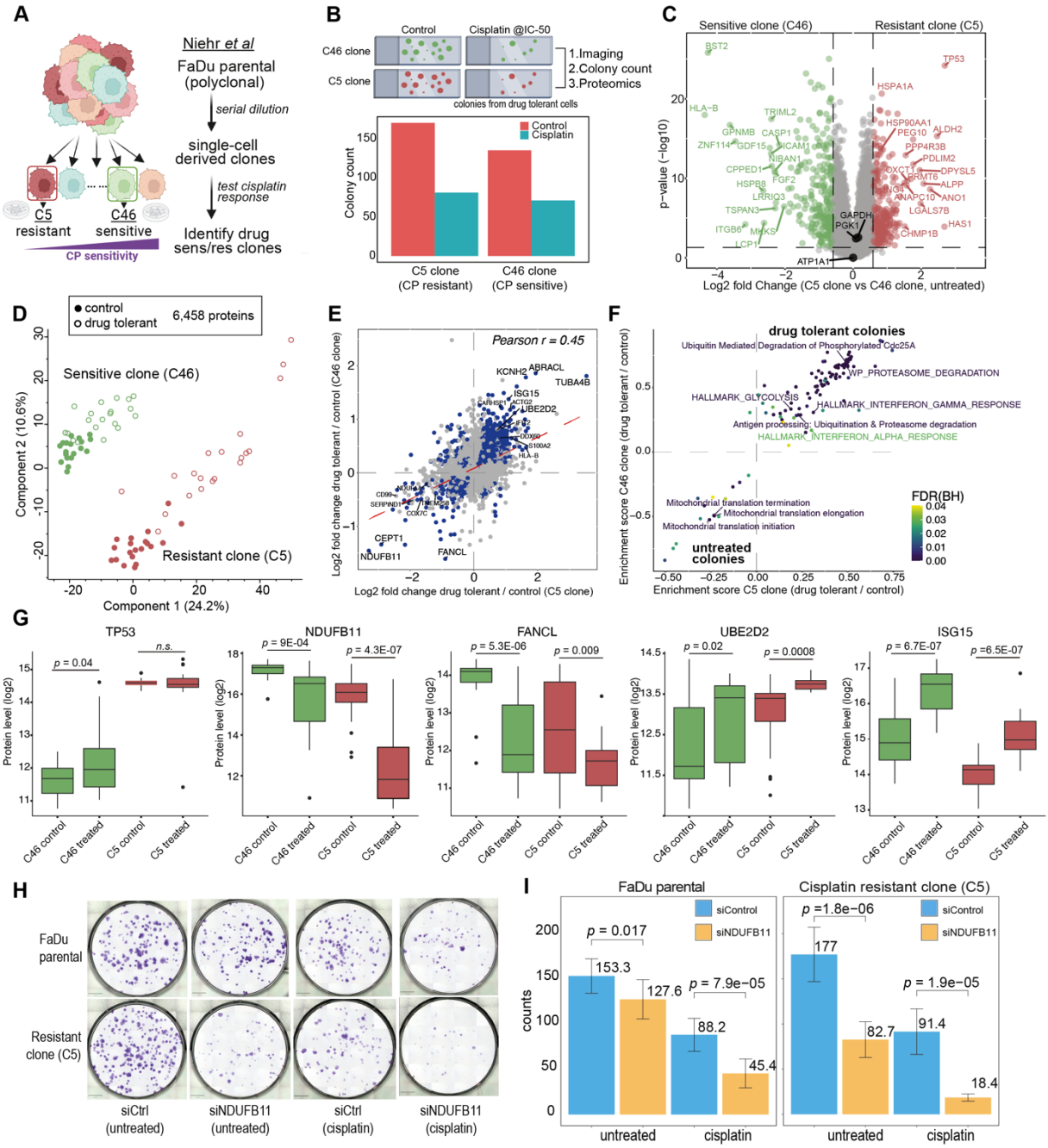

Fig. 3 PhenoSCoP captures genetic and non-genetic mechanisms of primary chemoresistance.
(A) Schematic representation of two previously characterized drug-naïve clones isolated from the FaDu parental cell line. Clone C5 showed higher primary cisplatin resistance than clone C46. **(B)** Top: Representative images of untreated and cisplatin-treated (IC_{50}) colonies grown on membrane slides. Bottom: Quantification of colony numbers for cisplatin-sensitive (C46) and cisplatin-resistant (C5) clones under untreated and respective IC_{50} treatment conditions. **(C)** Volcano plot comparing protein expression between C5 and C46 single cell-derived colonies. The stable housekeeping proteins GAPDH, PGK1, and ATP1A1 are depicted in black and do not show significant differential expression. **(D)** Principal component analysis (PCA) of resistant clone C5 (untreated n = 20, drug tolerant n = 20) and sensitive clone C46 (untreated n = 19, drug tolerant n = 20) colonies analyzed using PhenoSCoP. **(E)** Diagonal scatter plot comparing log_2 protein fold changes upon cisplatin treatment in resistant (C5, x-axis) versus sensitive (C46, y-axis) colonies, calculated as the ratio of treated to untreated cells for each clone. **(F)** Scatter plot

showing two-dimensional pathway enrichment scores for drug-tolerant C5 and C46 clones compared to their drug-naïve controls (FDR < 0.05). T-test statistics values (treated vs. untreated) were used as input for enrichment analysis. **(G)** Boxplot of protein levels for selected genes comparing drug-tolerant and drug-naïve colonies of clones 5 and 46. Significance was assessed by a two-sided Student's t-test. **(H)** Representative images from clonogenic assays showing the effects of NDUFB11 knockdown and cisplatin (CP) treatment on both parental and resistant (C5) FaDu cells. **(I)** Quantification of colonies from knockdown experiments is shown in panel H. Data represent the average number of colonies from three independent experiments. Significance was assessed by a two-sided Student's t-test.

PhenoSCoP identifies pre-existing proteotypes driving primary cisplatin resistance

Increasing evidence suggests that the cellular state prior to drug administration plays a crucial role in determining therapeutic responses [7,8,11]. Therefore, we next investigated whether PhenoSCoP could uncover the proteotypes associated with primary drug resistance. As both the C46 and C5 clones were derived from treatment-naïve FaDu parental cells, these proteotypes served as excellent ground truths to be picked using our method. To increase the likelihood of comparing different clones, we integrated fluorescence-based RGB barcoding, which is a powerful imaging-based technique for tracking individual clones *in vitro* and *in vivo* [49,50]. Through stochastic color mixing after lentiviral expression of different fluorescent proteins in varying but stable amounts, the RGB color profile serves as an inheritable marker and clonal fingerprint. This approach also enabled us to monitor clonal selection after long-term cyclic CP treatment and assess whether drug-resistant proteotypes were already pre-existing or developed through proteome remodelling.

To this end, FaDu parental cells were stably transduced with RGB vectors, enabling the visualization of diverse clonal populations (**Fig. 4A**). Following whole-slide RGB imaging using a widefield fluorescence microscope (**Fig. 4B**), we isolated 52 color-unique colonies and quantified over 7,200 proteins in total, with a median of more than 5,800 proteins per colony (**Fig. 4C**). Our dataset included many known oncogenes and tumor suppressors involved in HNSCC carcinogenesis, such as EGFR, TP53, BRCA1, and CDH2 (**Fig. 4D**). To systematically identify the most variable fraction of the proteome across single-cell-derived colonies, we plotted the coefficient of variation (CV) for each protein versus the mean protein abundance (**Fig. 4E**). To avoid potential bias from low-abundance proteins, which tended to exhibit higher variability, we binned the data into 100 segments and retained only the top 5% of each segment. Additionally, the 5% lowest-abundant proteins and those showing high variation in our mini-bulk controls were excluded. Using this strategy, we prioritized 357 variable proteins with high confidence. The protein sequence coverage of the selected proteins was similar to that of the full dataset (**Suppl.**

Fig. 4A), further supporting the idea that our approach prioritizes true biological and clone-specific signals rather than technical noise. An independent replicate dataset also confirmed a substantial overlap among the prioritized proteins, which was most pronounced at the pathway level (**Suppl. Fig. 4B**). We not only captured C5 and C46 clone-specific signatures, such as p53, DPYSL3, and the interferon-response proteins HLA-B, IFIT1, and DDX60 (**Fig. 4E**), but the quantified RGB reporter peptides (e.g., mTagBFP) also showed the expected variability, confirming that different clones were compared. Cell cycle-dependent (CCD) proteins [12] instead exhibited only low colony variation, consistent with their transient fluctuations (i.e., within one cell cycle) (**Suppl. Fig. 4C**). Repeated doses of CP led to strong clonal selection, as was evident from the dominant orange clone revealed by immunofluorescence imaging (**Suppl. Fig. 4D**). Interestingly, principal component analysis closely grouped drug-resistant clones with a small fraction of colonies derived from the untreated parental population. This finding was clearly obscured when we compared clonal mixtures (mini-bulk) (**Fig. 4F**), underlining the unique resolution of our method in identifying clone-specific molecular programs. P53, DPYSL3, CYP24A1, and N-cadherin (CDH2) were the most strongly elevated in these pre-resistant cells (**Fig. 4G-H**). Proteome correlation analysis further showed that the resistant proteotypes were highly related to a few drug-naïve parental clones (Pearson $r > 0.9$, **Fig. 4I**). While immunofluorescence (IF) imaging and RGB pseudo-color inference from reporter peptide quantification (**Suppl. Fig. 4E**) suggested that one dominant yellow/orange clone survived multiple rounds of CP (**Fig. 4H-I**), proteomics data revealed two distinct proteotypes of similar color (**Fig. 4I-K**). Although this observation could possibly be explained by one pre-resistant clone that underwent additional proteome remodelling after cyclic CP exposure, comparison with untreated cells of the same color-matched subcluster revealed no significant and quantifiable differences (**Fig. 4J)**. Both resistant clones in clusters 1 and 2 showed high mutant p53 levels and DNA damage repair signatures (**Fig. 4I and 4K)**, but with nuanced differences. While the resistant clone of cluster 1 was characterized by higher protein levels related to nucleotide excision repair, the main pathway for detecting and repairing CP-induced DNA adducts [51,52], the cluster 2 clone showed higher homologous recombination-based DNA damage repair and mitochondrial proteins (**Fig. 4K)**.

In summary, through PhenoSCoP*,* we identified and characterized pre-existing, rare proteotypes that dominated CP-resistant cell populations in the FaDu HNSCC model.

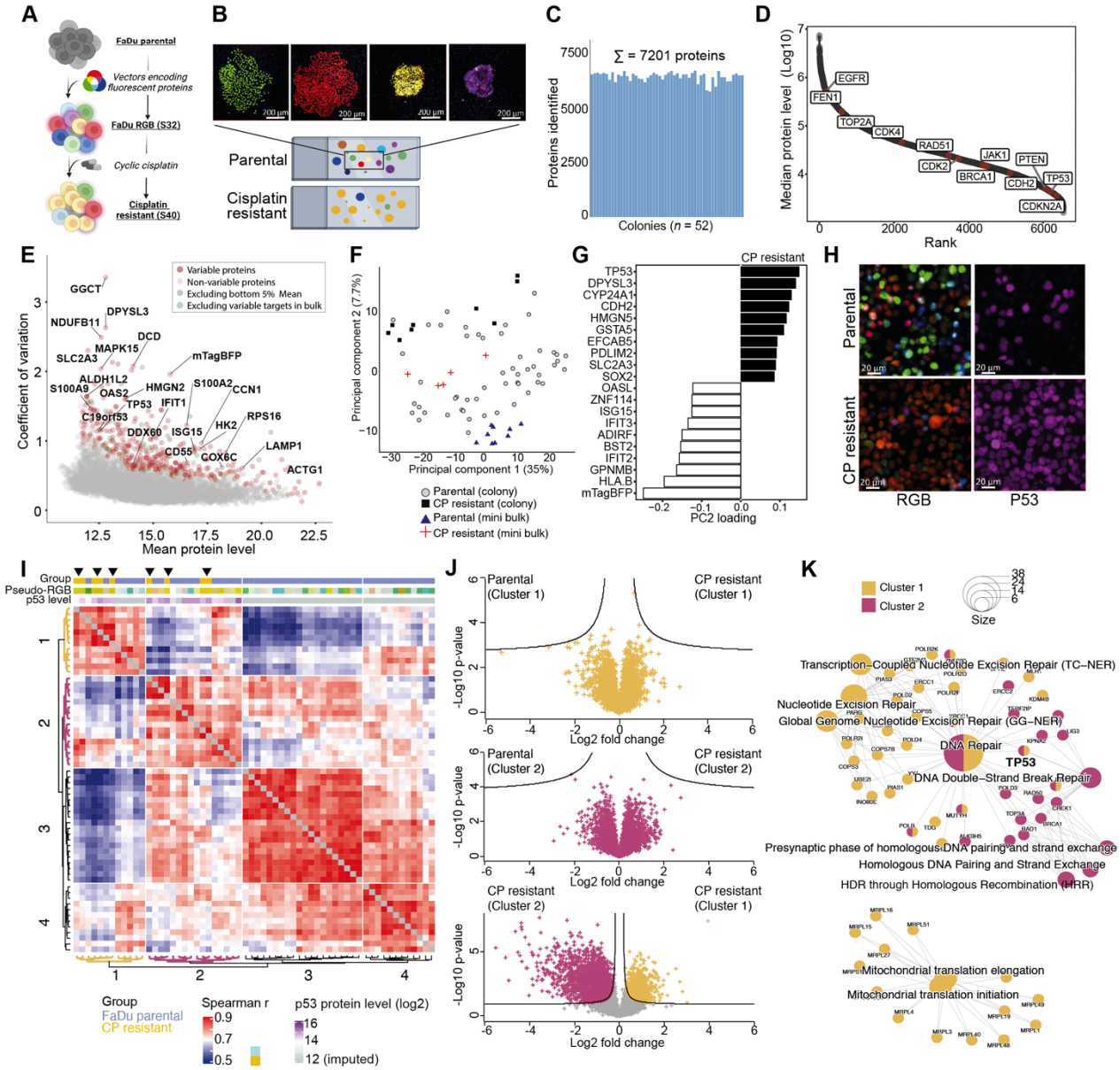

Fig. 4: PhenoSCoP identifies pre-existing proteotypes driving primary cisplatin resistance.
(A) Schematic of the lentiviral vector-mediated RGB-marked FaDu model system. **(B)** Representative images of colonies derived from single FaDU RGB clones. Scale bar: 200 µm. **(C)** Depth of 52 colony proteomic measurements. **(D)** Dynamic range of protein abundance from colony proteome measurements, with examples of oncogenes and tumor suppressor proteins highlighted. **(E)** Comparison of protein level variability (CV) and mean protein levels of all identified proteins. Variable proteins (red) are defined as the top 5% of the most variable proteins per binned segment. One hundred bins were used to cover the entire protein level range. Proteins with high variation in pseudo-bulk samples were excluded. **(F)** Principal component analysis (PCA) of FaDu primary clones (n = 52), primary mini-bulk samples (n = 9), resistant clones (n = 9), and resistant mini-bulk samples (n = 5) using 357 variable proteins. **(G)** Top 20 features contributing to principal component two of PCA in panel F. **(H)** Immunofluorescence staining of TP53 in primary and resistant FaDu cells. Scale bar: 20 µm. **(I)** Proteome correlation analysis based on the most variable proteins (related to panel E, filtered for 70% valid values). Distances were calculated using Euclidean metrics and hierarchical clustering using average linkage, revealing four main clusters. **(J)** Volcano plots comparing cisplatin-resistant versus drug-naive colonies from Cluster 1 (top) and Cluster 2 (middle). Bottom: Volcano plot comparing cisplatin-resistant colonies from Cluster 1 versus Cluster 2. Cluster information was extracted from panel I.

(K) Enriched Gene Ontology pathways of proteins significantly upregulated in cisplatin-resistant clones (panel I and J, clusters 1 and 2) compared to clusters 3 and 4, which included drug-naïve proteomes of FaDu parental cells.

Resistant proteotypes are present in patient-derived HNSCC tissues

To address whether the identified proteins and pathways associated with CP responses in the FaDu model also emerged in HNSCC patient tissues, we profiled a cohort of 29 HPV-negative, treatment-naïve HNSCC patients obtained from a previous phase III clinical trial of definitive radiochemotherapy (RCTx) for locally advanced HNSCC [53]. In this cohort, patients in the experimental arm received CP-based RCTx. Guided by H&E staining, we laser-microdissected tumor-specific regions of each tissue microarray core, quantifying ~ 6,500 proteins per sample (**Suppl. Fig. 5A**). Of the 357 variable proteins identified in the drug-naïve FaDu parental cells (**Fig. 4E**), which were associated with different clones and CP responses (**Fig. 4E-G**), 296 (82.9%) were also found in the patient tissue proteomes, illustrating their relevance *in vivo*. Compared to all identified proteins, our signature showed a clear and significant trend towards higher protein level variability across the 29 tumors (**Fig. 5C**, $p = 3.7 \times 10^{-8}$). The most variable proteins included aldehyde dehydrogenase ALDH3A1, interferon-related proteins (e.g., ISG15 and IFIT2), glutamine synthetase GLUL, and calcium-binding proteins from the S100 family (e.g., S100A8/A9), which have been implicated in epithelial differentiation and HNSCC progression through NF-κB and PI3K/Akt/mTOR signaling [54,55] (**Fig. 5D**). To assess whether these proteins also exhibited spatially related abundance differences, indicative of potential clone-specific proteotypes within distinct spatial niches, we compared the proteomes of several intra-tissue replicates from 29 patients (**Fig. 5D**). Indeed, compared to GAPDH, many of the most variable proteins (e.g., ALDH3A1, S100A8, IFIT2, and GLUL) also exhibited intra-tissue protein level variability of varying degrees (**Suppl. Fig. 5B**). For example, S100A8/A9 showed strong spatially related differences in patient 1, GLUL in patient 2, and ALDH3A1 was the most variable protein in patient 4. To test whether these proteins were also enriched in chemoresistant, recurring, or metastatic disease, we profiled an additional HNSCC case diagnosed as an aggressive, locally advanced squamous cell carcinoma of the mandible that recurred within six months after surgery with CP-based adjuvant RCtx and subsequently metastasized to multiple organs (**Suppl. Fig. 5C**). We profiled several tumor microregions (50,000 μm^2 per tissue region) from the primary tumor (n = 4), local recurrence (n = 4), lymph node metastasis (n = 4), and distant metastasis (paratracheal

[n = 4] and skin [n = 3]) to a depth of ~7,000 proteins per single measurement (**Fig. 5E**). Tissue proteomes showed strong tumor stage and anatomic site specificity, as revealed by principal component analysis (**Fig. 5F**). To determine which proteins and biological pathways were differentially abundant between the primary and recurrent tumors, we performed ANOVA coupled with pathway enrichment analysis. Notably, our FaDu-derived signature of variable proteins was significantly overrepresented among the proteins that showed abundance differences between the primary and metastatic tumors (**Fig. 5G-H**). Examples of these proteins included GLUL and DPYSL3, which were associated with the CP-resistant *TP53* mutant FaDu clone (**Fig. 4G**). At the pathway level, ribosomal proteins were upregulated in the relapse biopsy, as well as in the distant skin metastasis (**Fig. 5H**). This finding was consistent with our observations in the resistant C5 clone (**Suppl. Fig. 3D**). Instead, the primary tumor featured strong mesenchymal characteristics (e.g., epithelial-mesenchymal transition (EMT), and TGFβ signaling), as well as higher focal adhesion and PI3K/AKT pathway levels (**Fig 5I**).

Together, our data support the existence of diverse, spatially distinct proteotypes associated with chemoresistance, tumor progression, and metastasis in HNSCC patient samples. The observed overlap between our *in vitro* derived signatures and spatial tissue proteomics results underlines the translational relevance of the biological discoveries enabled by PhenoSCoP.

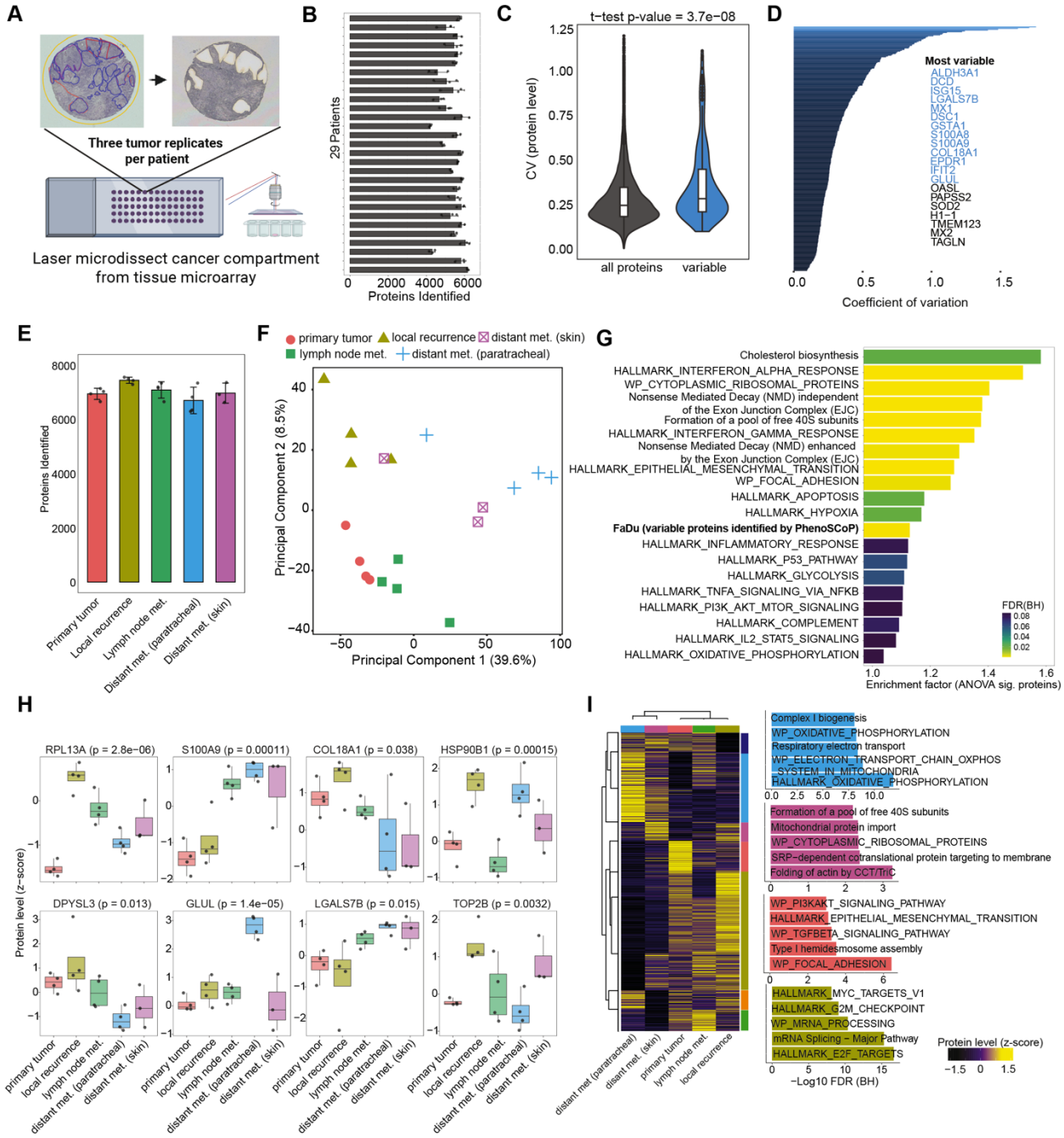

Fig 5: Proteotypes associated with differential cisplatin responses *in vitro* are present in HNSCC patient tissues **(A)** Schematic workflow of laser microdissection guided proteomics applied to tissue microarrays of patients with primary head and neck squamous cell carcinoma (HNSCC). Tumor-specific compartments were identified by H&E staining, with three replicates per tissue cut for proteome analysis. **(B)** Protein identification in tissue samples from 29 patients with head and neck cancer. **(C)** Boxplot of inter-patient protein coefficients of variation comparing all quantified proteins to the variable proteins identified using PhenoSCoP in the FaDu cell line model. **(D)** Ranked inter-patient coefficients of variation for variable proteins (from the in vitro FaDu cell model). Proteins with the highest variability are listed and marked in blue. **(E)** Barplot showing the number of proteins identified in multiple cancer tissue samples from a patient with relapse, including the primary tumor (n = 4), lymph node metastasis (n = 4), local recurrence (n = 4), and two distant metastases (paratracheal [n = 4] and skin [n = 3]). **(F)** Principal component analysis

(PCA) of multiple cancer tissue samples based on proteomic data. **(G)** Pathway enrichment analysis (Fisher's exact test) of significantly differentially expressed proteins across multiple cancer tissue samples (ANOVA, $p < 0.05$). Analyses were performed using the HALLMARK gene sets from the Human Molecular Signatures Database (MSigDB), Reactome, WikiPathways, and a custom list of variable proteins identified from the in vitro FaDu cell model using PhenoSCoP. **(H)** Boxplots showing the relative levels (z-scores) of the selected proteins across multiple cancer tissue samples. ANOVA p-values are indicated for each protein. **(I)** Heatmap of significantly differentially expressed proteins across multiple cancer tissue samples (ANOVA, $p < 0.05$). The heatmap shows the average protein abundance (row-wise z-score) for each tissue, and hierarchical clustering identifies seven gene clusters. Enrichment analysis of representative gene clusters identified in panel H. The top five significantly enriched pathways are shown for four clusters.

Discussion

Here, we introduce **Pheno**type-resolved **S**ingle-**Co**lony **P**roteomics (PhenoSCoP), a novel discovery proteomics approach that combines clonogenic cell growth, fluorescence microscopy, laser microdissection (LMD), and ultrasensitive mass spectrometry (MS)-based proteomics. It enables robust and deep proteome profiling through data-independent acquisition, yielding consistent and sufficient proteome coverage to comprehensively study oncogenic signaling pathways and biological processes associated with cellular treatment responses. Instead of analyzing single cells, we developed a scalable workflow to profile single-cell-derived colonies without extensive serial dilution experiments, focusing on small cell populations consisting of a few hundred cells. PhenoSCoP provides reliable protein quantification while preserving clonal heterogeneity, combining key strengths of bulk and single-cell proteomics. Moreover, it captures clone-specific and inherited genetic or non-genetic molecular traits. While cell cycle-regulated proteins showed minimal variation across colonies, we identified hundreds of proteins with significant differences in clone-specific abundances. For example, the identification of p53, DPYSL3, and GLUL among the most upregulated proteins in drug-resistant cells underscores their potential role in mediating cisplatin resistance. High GLUL levels can facilitate cancer cell survival in glutamine-depleted environments, such as those induced by genotoxic stress [56], through *de novo* glutamine synthesis [57]. DPYSL3 can act as a metabolic and DNA repair enhancer that promotes chemoresistance and poor outcomes [35,58]. The dominant upregulation of p53 aligns well with its established role in chemoresistance [39], proving that PhenoSCoP illuminates the molecular drivers of therapy resistance.

However, a current limitation of PhenoSCoP is that it might overlook transiently expressed proteins that may also play critical roles in immediate drug response mechanisms [59]. Future studies could incorporate dynamic sampling strategies to capture these transient changes and combine them with live-cell imaging to monitor clonal dynamics in a time-resolved manner. Moreover, despite being broadly applicable across cancer types and cellular models, our method requires adherent and proliferative cells that ultimately form colonies. Some cellular phenotypes are generally less proliferative or may not grow as colonies. These cells can be captured by single-cell laser microdissection as conceptualized in our recent deep visual proteomics method [60], independent of their capacity to grow out as colonies. While our method currently supports the imaging of 4-6 markers, multiplex immunofluorescence imaging [15] represents a promising future addition to our pipeline for more fine-resolved cell phenotyping to guide proteomic profiling.

A considerable advantage of integrating immunofluorescence microscopy and proteomics is the ability to study insightful phenotype-to-proteome associations. For example, EdU and DAPI staining provide important cell cycle information. Applying this strategy, we discovered rare phenotypes of slow- or fast-cycling cells that are likely to be missed by current single cell or bulk proteomics approaches. RGB fluorescent barcoding is another powerful addition to our method and adds a new dimension for clonal tracking and deconvolution of proteomic data. We devised an MS-based approach to directly quantify RGB reporter peptides to infer pseudo-colors for clonal tracking. This approach could also be highly relevant in microscopy-free setups, for example, for clonally deconvoluting SCP data. Combined with drug treatment assays, this RGB strategy enabled us to identify distinct proteotypes associated with primary cisplatin resistance in drug-naive FaDu cells. Although initially rare, these proteotypes strongly dominated the resistant populations after multiple rounds of cisplatin exposure. Notably, our rich proteomic data also indicated that long-term drug exposure had only a minimal effect on the quantitative proteome of these clones, underlining the importance of studying clonal proteomic heterogeneity before treatment to better understand the biological mechanisms underlying therapeutic responses.

The ability of PhenoSCoP to identify pre-existing resistant proteotypes offers a new avenue for the development of predictive biomarkers, potentially enabling the stratification of patients who are likely to benefit from cisplatin therapy. The clinical relevance of our *in vitro* findings is supported

by the observation that proteins that varied across cultured colonies also showed intra- and inter-tumor heterogeneity in primary head and neck squamous cell carcinoma (HNSCC) tissues. Our spatially resolved proteomic analysis of patient-matched primary and relapsed HNSCC tumor samples revealed that several of these proteins were upregulated upon disease recurrence and metastasis. An interesting finding that emerged in both the FaDu model and the relapsed HNSCC case was the upregulation of ribosomal proteins in chemoresistant cells and disease progression. This finding suggests a potential role in drug resistance and disease progression [61]. Future studies could explore the functional significance of these (onco)ribosomal protein changes and their potential as therapeutic targets and oncogenic signaling mediators [62]. Additionally, investigating the mechanisms underlying proteomic changes observed during disease recurrence and metastasis could provide valuable insights into HNSCC progression and guide the development of more effective treatment strategies.

In summary, PhenoSCoP is a powerful and versatile discovery tool for dissecting intratumoral heterogeneity and drug resistance mechanisms. The ability to identify hereditary, clone-specific proteomic signatures associated with treatment responses addresses the key limitations of current single-cell and bulk proteomic approaches. Further development and application of this method may reveal new predictive biomarkers and therapeutic vulnerabilities for improving cancer treatment.

Author contributions

Conceptualization, D.Q. and F.C.; methodology, D.Q., S.S., R.D., K.R.; experiments, D.Q., R.D.; data curation, D.Q., S.S., I.T., F.C.; data analysis, D.Q. and F.C.; figures, D.Q., and F.C.; supervision, I.T. and F.C.; funding acquisition, K.R., I.T. and F.C.; writing the original draft, F.C. All authors reviewed and edited the manuscript.

The authors declare no conflicts of interest.

Acknowledgments

We thank our colleagues at the Max Delbrück Center (MDC) and Charité for their support and fruitful discussions. In particular, Daniela Valdes and Bella Banjanin for their feedback on the manuscript. We also thank Gina Dörpholz, Pia Larsen and Jeannine Engel for administrative support. D.Q., F.C., I.T., and S.S. acknowledge funding support from the Federal Ministry of Education and Research (BMBF), as part of the National Research Initiatives for Mass Spectrometry in Systems Medicine, under grant agreement No. 161L0222 and 16LW0239K (Charité – University Medicine Berlin) of funding phase B, that is MSTARS-2. This project received funding from the European Research Council (ERC) under the European Union's Horizon 2020 Research and Innovation Program (grant agreement No. 101115681) and was supported by the ERC (ERC starting grant). I.T. and K.R. acknowledge the funding from the Deutsche Forschungsgemeinschaft (DFG, German Research Foundation, TI 929/3-1, RI 2927/1-1).

References

1. Vasan, N., Baselga, J. & Hyman, D. M. A view on drug resistance in cancer. *Nature* **575**, 299–309 (2019).
2. McGranahan, N. & Swanton, C. Clonal Heterogeneity and Tumor Evolution: Past, Present, and the Future. *Cell* vol. 168 613–628 Preprint at https://doi.org/10.1016/j.cell.2017.01.018 (2017).
3. Dagogo-jack, I. & Shaw, A. T. Tumour heterogeneity and resistance to cancer therapies. *Nature Publishing Group* **15**, 81–94 (2017).
4. Marine, J. C., Dawson, S. J. & Dawson, M. A. Non-genetic mechanisms of therapeutic resistance in cancer. *Nature Reviews Cancer 2020 20:12* **20**, 743–756 (2020).
5. Nam, A. S., Chaligne, R. & Landau, D. A. Integrating genetic and non-genetic determinants of cancer evolution by single-cell multi-omics. *Nat Rev Genet* **22**, 3–18 (2021).
6. Aebersold, R. & Mann, M. Mass-spectrometric exploration of proteome structure and function. *Nature* vol. 537 347–355 Preprint at https://doi.org/10.1038/nature19949 (2016).
7. Goyal, Y. *et al.* Diverse clonal fates emerge upon drug treatment of homogeneous cancer cells. *Nature* **620**, 651–659 (2023).
8. Schaff, D. L., Fasse, A. J., White, P. E., Vander Velde, R. J. & Shaffer, S. M. Clonal differences underlie variable responses to sequential and prolonged treatment. *Cell Syst* **15**, 213-226.e9 (2024).
9. Sydney Shaffer, A. M. *et al.* Memory Sequencing Reveals Heritable Single-Cell Gene Expression Programs Associated with Distinct Cellular Behaviors. https://doi.org/10.1016/j.cell.2020.07.003 (2020) doi:10.1016/j.cell.2020.07.003.
10. Rambow, F. *et al.* Toward Minimal Residual Disease-Directed Therapy in Melanoma. *Cell* **174**, 843-855.e19 (2018).
11. Kim, C. *et al.* Chemoresistance Evolution in Triple-Negative Breast Cancer Delineated by Single-Cell Sequencing. *Cell* **173**, 879-893.e13 (2018).
12. Mahdessian, D. *et al.* Spatiotemporal dissection of the cell cycle with single-cell proteogenomics. *Nature* **590**, 649–654 (2021).
13. Cohen, A. A. *et al.* Dynamic proteomics of individual cancer cells in response to a drug. *Science (1979)* **322**, 1511–1516 (2008).
14. Snijder, B. *et al.* Image-based ex-vivo drug screening for patients with aggressive haematological malignancies: interim results from a single-arm, open-label, pilot study. *Lancet Haematol* **4**, e595–e606 (2017).
15. Lin, J. R., Fallahi-Sichani, M. & Sorger, P. K. Highly multiplexed imaging of single cells using a high-throughput cyclic immunofluorescence method. *Nature Communications 2015 6:1* **6**, 1–7 (2015).
16. Mills, C. E. *et al.* Multiplexed and reproducible high content screening of live and fixed cells using Dye Drop. *Nat Commun* **13**, 1–18 (2022).
17. Bennett, H. M., Stephenson, W. & Rose, C. M. Single-cell proteomics enabled by next-generation sequencing or mass spectrometry. *Nat Methods* https://doi.org/10.1038/s41592-023-01791-5 (2023) doi:10.1038/s41592-023-01791-5.

18. Geiger, T. Tackling tumor complexity with single-cell proteomics. **20**, 324–326 (2023).
19. Leduc, A., Huffman, R. G., Cantlon, J., Khan, S. & Slavov, N. Exploring functional protein covariation across single cells using nPOP. *Genome Biol* **23**, 1–31 (2022).
20. Ye, Z. *et al.* Enhanced sensitivity and scalability with a Chip-Tip workflow enables deep single-cell proteomics. *Nat Methods* https://doi.org/10.1038/s41592-024-02558-2 (2025) doi:10.1038/s41592-024-02558-2.
21. Brunner, A. *et al.* Ultra-high sensitivity mass spectrometry quantifies single-cell proteome changes upon perturbation. *Mol Syst Biol* **18**, (2022).
22. Gatto, L. *et al.* Initial recommendations for performing, benchmarking, and reporting single-cell proteomics experiments. **20**, 375–386 (2022).
23. Bubis, J. A. *et al.* Challenging the Astral mass analyzer - up to 5300 proteins per single-cell at unseen quantitative accuracy to study cellular heterogeneity. *bioRxiv* 2024.02.01.578358 (2024) doi:10.1038/s41592-024-02559-1.
24. Woo, J. *et al.* Single-Cell Proteomic Characterization of Drug-Resistant Prostate Cancer Cells Reveals Molecular Signatures Associated with Morphological Changes. *Molecular & Cellular Proteomics* **24**, 100949 (2025).
25. Mold, J. E. *et al.* Clonally heritable gene expression imparts a layer of diversity within cell types. *bioRxiv* 2022.02.14.480352 (2022) doi:10.1016/j.cels.2024.01.004.
26. Sigal, A. *et al.* Variability and memory of protein levels in human cells. *Nature* **444**, 643–646 (2006).
27. Spencer, S. L., Gaudet, S., Albeck, J. G., Burke, J. M. & Sorger, P. K. Non-genetic origins of cell-to-cell variability in TRAIL-induced apoptosis. *Nature* **459**, 428–432 (2009).
28. PUCK, T. T. & MARCUS, P. I. Action of x-rays on mammalian cells. *Volume 103, Issue 5, Pages 653 - 666* **103**, 653–666 (1956).
29. Brix, N., Samaga, D., Belka, C., Zitzelsberger, H. & Lauber, K. Analysis of clonogenic growth in vitro. *Nat Protoc* **16**, 4963–4991 (2021).
30. Rangan, S. R. S. A new human cell line (FaDu) from a hypopharyngeal carcinoma. *Cancer* **29**, 117–121 (1972).
31. Piga, I., Koenig, C., Lechner, M., Sabatier, P. & Olsen, J. V. Formaldehyde Fixation Helps Preserve the Proteome State during Single-Cell Proteomics Sample Processing and Analysis. *J Proteome Res* **24**, 1624–1635 (2025).
32. Meier, F. *et al.* diaPASEF: parallel accumulation–serial fragmentation combined with data-independent acquisition. *Nat Methods* **17**, 1229–1236 (2020).
33. Demichev, V., Messner, C. B., Vernardis, S. I., Lilley, K. S. & Ralser, M. DIA-NN: neural networks and interference correction enable deep proteome coverage in high throughput. *Nat Methods* **17**, 41–44 (2020).
34. Ly, T. *et al.* Proteomic analysis of cell cycle progression in asynchronous cultures, including mitotic subphases, using PRIMMUS. *Elife* **6**, 1–35 (2017).
35. Matsunuma, R. *et al.* DPYSL3 modulates mitosis, migration, and epithelial-to-mesenchymal transition in claudin-low breast cancer. *Proc Natl Acad Sci U S A* **115**, E11978–E11987 (2018).
36. Tsherniak, A. *et al.* Defining a Cancer Dependency Map. *Cell* **170**, 564-576.e16 (2017).
37. Johnson, D. E. *et al.* Head and neck squamous cell carcinoma. *Nat Rev Dis Primers* **6**, (2020).

38. Nör, C. *et al.* Cisplatin induces Bmi-1 and enhances the stem cell fraction in head and neck cancer. *Neoplasia (United States)* **16**, 137–146 (2014).
39. Niehr, F. *et al.* Multilayered omics-based analysis of a head and neck cancer model of cisplatin resistance reveals intratumoral heterogeneity and treatment-induced clonal selection. *Clinical Cancer Research* **24**, 158–168 (2018).
40. Sharma, A. *et al.* Longitudinal single-cell RNA sequencing of patient-derived primary cells reveals drug-induced infidelity in stem cell hierarchy. *Nat Commun* **9**, (2018).
41. Tinhofer, I. *et al.* Targeted next-generation sequencing of locally advanced squamous cell carcinomas of the head and neck reveals druggable targets for improving adjuvant chemoradiation. *Eur J Cancer* **57**, 78–86 (2016).
42. Tanaka, N. *et al.* Gain-of-function mutant p53 promotes the oncogenic potential of head and neck squamous cell carcinoma cells by targeting the transcription factors FOXO3a and FOXM1. *Oncogene* **37**, 1279–1292 (2018).
43. Amlani, L. *et al.* Expression of P53 and Prognosis in Patients with Head and Neck Squamous Cell Carcinoma (HNSCC). *Int J Cancer Clin Res* **6**, (2019).
44. Boysen, M., Kityk, R. & Mayer, M. P. Hsp70- and Hsp90-Mediated Regulation of the Conformation of p53 DNA Binding Domain and p53 Cancer Variants. *Mol Cell* **74**, 831-843.e4 (2019).
45. Zylicz, M., King, F. W. & Wawrzynow, A. Hsp70 interactions with the p53 tumour suppressor protein. *EMBO J* **20**, 4634–4638 (2001).
46. Barkley, D. *et al.* Cancer cell states recur across tumor types and form specific interactions with the tumor microenvironment. *Nature Genetics 2022 54:8* **54**, 1192–1201 (2022).
47. Weichselbaum, R. R. *et al.* An interferon-related gene signature for DNA damage resistance is a predictive marker for chemotherapy and radiation for breast cancer. *Proc Natl Acad Sci U S A* **105**, 18490–18495 (2008).
48. Salovska, B. *et al.* A robust multiplex-DIA work fl ow pro fi les protein turnover regulations associated with cisplatin resistance and aneuploidy. https://doi.org/10.1038/s41467-025-60319-x (2025) doi:10.1038/s41467-025-60319-x.
49. Weber, K. *et al.* RGB marking facilitates multicolor clonal cell tracking. *Nature Medicine 2011 17:4* **17**, 504–509 (2011).
50. Cornils, K. *et al.* Multiplexing clonality: Combining RGB marking and genetic barcoding. *Nucleic Acids Res* **42**, (2014).
51. Wood, R. D. Nucleotide excision repair in mammalian cells. *Journal of Biological Chemistry* **272**, 23465–23468 (1997).
52. Lemaire, M. A., Schwartz, A., Rahmouni, A. R. & Leng, M. Interstrand cross-links are preferentially formed at the d(GC) sites in the reaction between cis-diamminedichloroplatinum (II) and DNA. *Proceedings of the National Academy of Sciences* **88**, 1982–1985 (1991).
53. Budach, V. *et al.* Five years' results of the German ARO 04-01 trial of concurrent 72 Gy hyperfractionated accelerated radiation therapy (HART) plus once weekly cisplatinum/5-FU versus mitomycin C/5-FU in stage IV head and neck cancer. *Journal of Clinical Oncology* **30**, 5512–5512 (2012).
54. Zhou, H., Zhao, C., Shao, R., Xu, Y. & Zhao, W. The functions and regulatory pathways of S100A8/A9 and its receptors in cancers. *Front Pharmacol* **14**, 1187741 (2023).

55. Argyris, P. P. *et al.* Intracellular calprotectin (S100A8/A9) controls epithelial differentiation and caspase-mediated cleavage of EGFR in head and neck squamous cell carcinoma. *Oral Oncol* **95**, 1–10 (2019).
56. Jin, J., Byun, J. K., Choi, Y. K. & Park, K. G. Targeting glutamine metabolism as a therapeutic strategy for cancer. *Exp Mol Med* **55**, 706–715 (2023).
57. Bayram, Şafak *et al.* Investigating the role of GLUL as a survival factor in cellular adaptation to glutamine depletion via targeted stable isotope resolved metabolomics. *Front Mol Biosci* **9**, 1–12 (2022).
58. Kaarijärvi, R., Kaljunen, H., Itkonen, N., Bureiko, K. & Ketola, K. DPYSL3B is a regulator of chemoresistance via DNA repair and metabolic reprogramming in prostate cancer. *bioRxiv* 2025.07.03.658029 (2025) doi:10.1101/2025.07.03.658029.
59. Meyer, M. *et al.* Profiling the Non-genetic Origins of Cancer Drug Resistance with a Single-Cell Functional Genomics Approach Using Predictive Cell Dynamics. *Cell Syst* **11**, 367-374.e5 (2020).
60. Mund, A. *et al.* Deep Visual Proteomics defines single-cell identity and heterogeneity. *Nature Biotechnology 2022 40:8* **40**, 1231–1240 (2022).
61. Elhamamsy, A. R., Metge, B. J., Alsheikh, H. A., Shevde, L. A. & Samant, R. S. Ribosome Biogenesis: A Central Player in Cancer Metastasis and Therapeutic Resistance. *Cancer Res* **82**, 2344–2353 (2022).
62. Kang, J. *et al.* Ribosomal proteins and human diseases: molecular mechanisms and targeted therapy. *Signal Transduct Target Ther* **6**, 1–22 (2021).
63. Mohme, M. *et al.* Optical Barcoding for Single-Clone Tracking to Study Tumor Heterogeneity. *Molecular Therapy* **25**, 621–633 (2017).
64. Makhmut, A. *et al.* A framework for ultra-low-input spatial tissue proteomics. *Cell Syst* **14**, 1002-1014.e5 (2023).
65. Ctortecka, C. *et al.* Automated single-cell proteomics providing sufficient proteome depth to study complex biology beyond cell type classifications. *Nat Commun* **15**, 1–10 (2024).
66. Perez-Riverol, Y. *et al.* The PRIDE database and related tools and resources in 2019: Improving support for quantification data. *Nucleic Acids Res* **47**, D442–D450 (2019).

Methods and Materials

HNSCC patient tissue collection

Primary cancer patient samples were obtained from a multicenter phase III trial (ARO-0401) conducted between 2004 and 2008. All the samples included in this study (n = 29) were HPV-negative treatment-naïve tumors. Multiple tumor specimens from the recurrent patient (HPV-negative) were collected between 2022 and 2023 during surgery, including the primary tumor, lymph node metastasis, local recurrence, and distant metastases to the skin and paratracheal region. All tissue blocks were stored at room temperature in the archive of the Institute of Pathology at Charité University Hospital, Campus Benjamin Franklin. The study was performed according to the ethical principles for medical research of the Declaration of Helsinki, and approval was obtained from the Ethics Committee of the Charite´ University Medical Department in Berlin (EA1/222/21). Informed consent was obtained from all participants included in the study.

Cell lines

The hypopharyngeal tumor cell line FaDu (ATCC®HTB–43™) was purchased from ATCC (Manassas, VA, USA). FaDu clonal cell lines (C5 and C46) were obtained from the laboratory of Prof. Dr. Ingeborg Tinhofer-Keilholz [39]. The cells were cultured in Minimum Essential Medium (MEM) supplemented with 12% fetal bovine serum (FBS), 1× non-essential amino acids (NEAA), and penicillin/streptomycin (penicillin/streptomycin). Cells were regularly tested for mycoplasma by PCR.

Transduction of Fadu cells with RGB

Fadu cells were transduced with the lentiviral vectors LeGO-B2-NLS-Puro+, LeGO-V2-NLS-Puro+, and LeGO-C2-NLS-Puro+ for RGB nuclear barcoding, followed by molecular barcoding with LeGO-EBFP2-Hygro-LTRXX3-BC24 for clonal tracking. Dr. Kristoffer Riecken from the University Hospital Hamburg-Eppendorf provided all virus particles [63]. For transduction, 50,000 cells per well were seeded in a 24-well plate (Greiner Bio-One #353047). Cells were incubated for 2-5 hours to facilitate cell attachment. The medium was replaced with polybrene-containing medium (8 µg/mL), and lentiviral particles were added to the wells. Spinoculation (1,000 × g, 1 h,

25 °C) was performed on the plate, and cells were incubated for another 16 h. The medium was then exchanged for a regular, non-polybrene-containing medium.

The efficiency of RGB transduction was determined by flow cytometry. The most efficient transduction combination (all three 3 vectors) was used for molecular barcoding. The efficiency of molecular barcoding was determined by ddPCR using the ratio of Hygro/FAM9B. A ratio of 1 or the closest to 1 was used for further experiments with irradiation (IRR) and drug treatment.

Colony growth for PhenoSCoP

Steel-frame PPS (polyphenylene sulfide) membrane slides (Leica, #11600294) and 12 mm round glass coverslips were sterilized by exposure to ultraviolet (UV) light for 30 min before use. They were then incubated with 0.1 mg/mL poly-L-lysine (Sigma #P1274) at 37°C for 30 min, rinsed once with sterilized water, and allowed to dry under UV light. For seeding, 4,000–5,000 cells were placed into a 10 cm cell culture dish containing a single PPS slide, while approximately 500 cells were seeded into each well of a 24-well plate, each containing a sterilized coverslip. The culture medium was replaced every 2–3 days to ensure optimal cell growth.

Drug treatment

Cells were seeded onto membrane slides and incubated overnight at 37°C to allow cell attachment. The following day, cells were treated with cisplatin at concentrations corresponding to their individual IC_{50} values for 24 h. After treatment, the cells were washed once with phosphate-buffered saline (PBS), and fresh drug-free medium was added. The medium was replaced at regular intervals to support colony growth.

For cyclic CP treatment, 30,000 FaDu cells were seeded in each well of a 6-well plate. Cells were treated with four doses of 100 ng/ml and four doses of 150 ng/ml, with a cumulative dose of 1000 ng/ml. Cells were split and reseeded after every cisplatin dose and harvested for further experiments. The drug used for drug testing included cisplatin (NeoCorp GmbH, Germany).

SiRNA transfection

siRNA pools (siPOOLs) were obtained from siTOOLs Biotech GmbH. Gene knockdown was performed in untreated FaDu parental cells and the cisplatin-resistant clone (C5) using either control siRNA (siCTRL) or an siPOOL targeting NDUFB11, according to the manufacturer's instructions. Briefly, 240,000 cells were seeded per well in 6-well plates and allowed to adhere overnight prior to transfection. Cells were transfected with 3 nM siRNA and incubated for 48 h. For the clonogenic assay, 500 cells were seeded per condition.

Immunofluorescence microscopy

After 8–10 days of growth, colonies were fixed with 4% paraformaldehyde (PFA, Thermo Scientific, # 28908) for 10 min at room temperature. A silicon frame (0.5 mm thickness, Technikplaza GmbH) was mounted onto the slide to facilitate the subsequent steps. Immunofluorescence staining was performed on PPS slides. In brief, cells and colonies were permeabilized by adding 90% cold methanol (in 10% PBS) for 2 min. After thoroughly washing away the methanol, Odyssey Blocking Buffer PBS (Li-Cor, 927-40000) was applied to block non-specific binding sites for 30 min at room temperature. Antibodies were diluted to optimal concentrations in blocking buffer and incubated with the cells overnight at 4°C. When unconjugated primary antibodies were used, a secondary antibody was added and incubated for 1 h at room temperature. Hoechst 33342 (Thermo Scientific, # 62249) was applied for 10 min at room temperature for nuclear staining. Images were acquired using an Axioscan 7 (Carl Zeiss Microscopy GmbH, Germany) with a 10x objective. The optimal antibody concentrations used were as follows: Na/K ATPase (1:500, Abcam, # 76020), panCK (1:100, Thermo Fisher Scientific, 41-9003-82), DDX60 (1:20, Novus, NBP1-91826), TP53 (1:50, Agilent Dako, M7001), and Ki-67 (1:100, Cell Signaling Technology, #11882). The secondary antibodies used were goat anti-mouse (1:500, Alexa Fluor™ 750, Thermo Fisher Scientific, A-21037) and goat anti-rabbit (1:1000, Alexa Fluor™ 488, Thermo Fisher Scientific). EdU staining was performed using a commercial kit according to the manufacturer's instructions (Thermo Fisher Scientific, C10338).

Colony isolation and proteomic sample preparation

Colony selection was performed using QuPath (v0.5.1) and exported to LMD using an in-lab pipeline (https://github.com/CosciaLab/Qupath_to_LMD). LMD7 (Leica Microsystems,

Germany) was used to isolate the colonies. Sample preparation for colony and patient samples was performed based on our previous work [64]. Briefly, samples in 384-well plates were lysed with 2 µL of lysis buffer consisting of 0.1% DDM, 5 mM TCEP, 20 mM CAA, and 100 mM TEAB at 95 °C for 1 h. Sequential digestion was applied by adding 1 µL of LysC (2 ng) and incubating for 4 h, followed by the addition of 1 µL of trypsin (2 ng) and overnight incubation at 37 °C. All buffers were added using a liquid dispenser (MANTIS, Formulatrix) for better accuracy. Peptides were desalted using Evotips (Evosep Biosystems, Denmark) according to the manufacturer's instructions.

Single-cell proteomics

Single FaDu cells were sorted and prepared using the CellenONE system (Cellenion) on proteoCHIP EVO 96 plates according to an adapted published protocol [65]. Briefly, 3 µL of hexadecane was added to each well prior to cell sorting, followed by dispensing 150 nL of Master Mix (0.2% DDM, 100 mM TEAB, and 10 ng/µL trypsin) into each well. During lysis and enzymatic digestion, the on-deck temperature was maintained at 50 °C, with continuous rehydration of samples by adding 60 nL H_2O at 2-minute intervals for 2 h. Subsequently, the samples were loaded onto Evotips by centrifugation.

Liquid chromatography-mass spectrometry (LC-MS/MS)

LC-MS/MS was performed using timsTOF Ultra/Ultra 2 mass spectrometers (Bruker Daltonics, Germany) coupled to an EASYnLC-1200 system (Thermo Fisher Scientific, USA). Peptide separation was conducted on 20 cm home-packed columns (75 µm inner diameter) packed with 1.9 µm ReproSil-Pur C18-AQ silica beads (Dr. Maisch GmbH, Germany). A 21-minute gradient was used for peptide separation, employing buffer A (3% acetonitrile [ACN], 0.1% formic acid) and buffer B (90% ACN, 0.1% formic acid). The gradient was initiated at 2% buffer B and increased to 10% over 1.5 minutes at a flow rate of 0.4 µL/min to minimize dead time at the start of chromatography. Subsequently, the flow rate was reduced to 0.25 µL/min, and buffer B was ramped up to 60% over 15 min, followed by a washing step at 90% buffer B. All mass spectrometric analyses were conducted using the dia-PASEF method [32], employing the factory default settings in high sensitivity mode. Eight dia-PASEF windows were distributed across three trapped ion mobility spectrometry (TIMS) scans, covering an m/z range of 400 to 1,000. The ion

mobility range was set from 0.64 to 1.37 Vs cm^{-2}, with an accumulation and ramp time of 100 ms.

Primary patient samples were measured using the Evosep ONE 30 SPD system with a 15 cm column (EV1106). Multi-cancer samples from the recurrent patient and single-cell samples were analyzed using the Whisper Zoom 40 SPD system (Evosep) equipped with an Aurora Elite column (15 × 75 µm, 1.7 µm).

Raw file analysis

We used DIA-NN [33] (versions 1.8.1 and 1.9) for proteome quantification. Colony and patient samples were searched against an in silico spectral library generated from the UniProt human reference proteome (2023 release) supplemented with a FASTA file containing common contaminants. In addition, three color vector sequences (RGB) were included in the library to enable RGB sample identification. For single-cell samples, a FaDu cell–specific spectral library was generated using eight fractions of pooled cell lysate. Carbamidomethylation of cysteine residues was specified as a fixed modification, whereas oxidation of methionine was included as a variable modification. The maximum number of missed cleavages and variable modifications per peptide was set to one. Match-between-runs (MBR) functionality was enabled for all analyses.

Data analysis

Data analysis was carried out using the pg.matrix output file of DI-ANN with a global protein FDR of max. 1%. Perseus (v1.6.15.0) and R (v4.4.1) were used for further data analysis. The following R packages were used: tidyverse (2.0.0), ggplot2 (4.0.0), dplyr (1.1.4), cluster (2.1.8.1), factoextra (1.0.7), stringr (1.5.1), tidyr (1.3.1), clusterProfiler (4.15.1.2), doBy (4.7.0), ComplexHeatmap (2.20.0), circlize (0.4.16).

Variable proteins in primary FaDu cells were calculated as follows: The data were filtered to retain proteins with at least five valid replicates. The intensity values were then log2-transformed to prepare for the imputation of missing values. Missing values were replaced by sampling from a normal distribution. The coefficient of variation (CV) was calculated in linear space, while the mean expression level for each protein was log-transformed. To obtain variable proteins across the whole dynamic range, the mean expression levels of proteins across colonies were divided into 100 bins. The top 5% of proteins with the highest CV were selected from each bin. Low-intensity

proteins below 5% of the colony mean distribution were removed to reduce the influence of technical noise on the results. Proteins were excluded if their CV in mini-bulk samples was larger than that of the colony samples.

Declaration of generative AI and AI-assisted technologies in the writing process

During the preparation of this manuscript, the authors used Paperpal in order to improve readability and language of the text. After using this tool, the authors reviewed and edited the content as needed and take full responsibility for the content of the publication.

Data availability

The mass spectrometry proteomics data have been deposited to the ProteomeXchange Consortium (http://proteomecentral.proteomexchange.org) via the PRIDE partner [66] and will be available upon acceptance of the manuscript. Any additional information required to reanalyze the data reported in this paper is available from the lead contact upon request.

Supplementary Figures

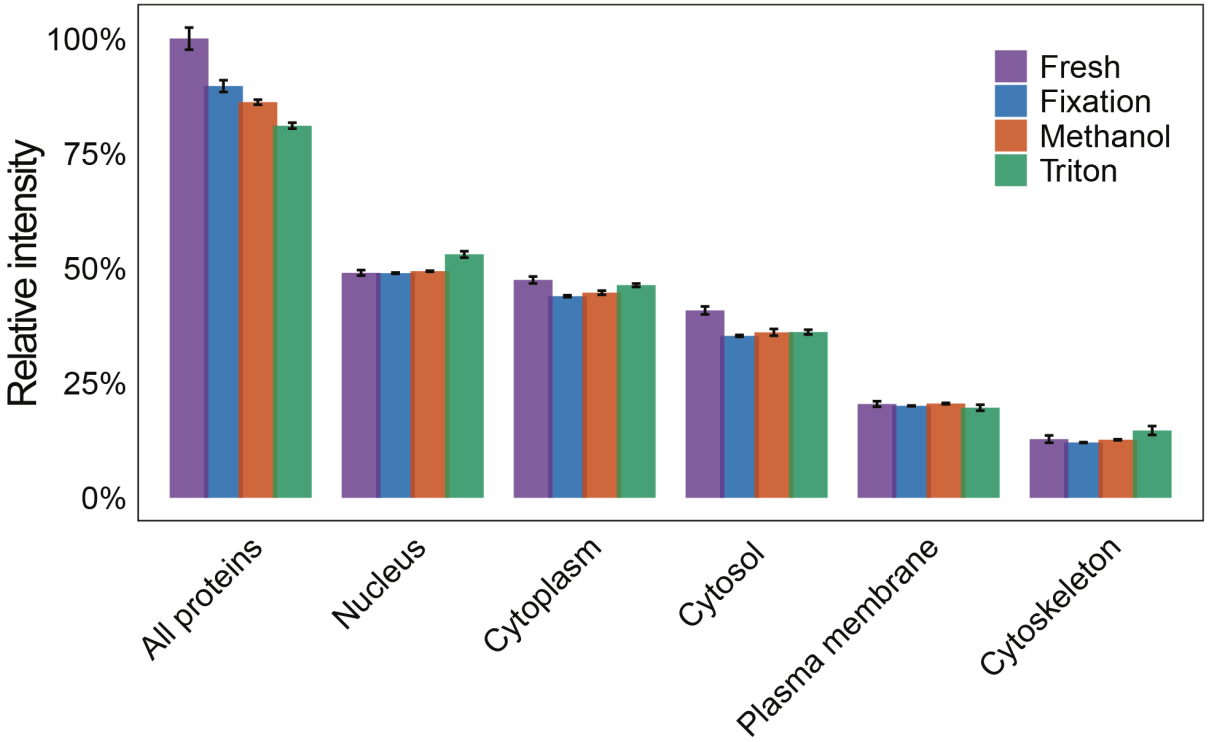

Fig. S1, related to Fig. 1. Comparison of summed intensity ratios from different cellular compartments across four experimental conditions: Fresh cells, formaldehyde fixed cells (FA, fixation), FA fixed cells and permeabilized cells based on ice-cold methanol (Methanol) and Triton-X-100 (Triton). 'Sum' represents the total intensity of proteins shared across all conditions (normalized to the average intensity of fresh cells). Other cellular compartments represent the summed intensity of proteins assigned to Gene Ontology Cellular Component groups (normalized to the total protein intensity of each sample).

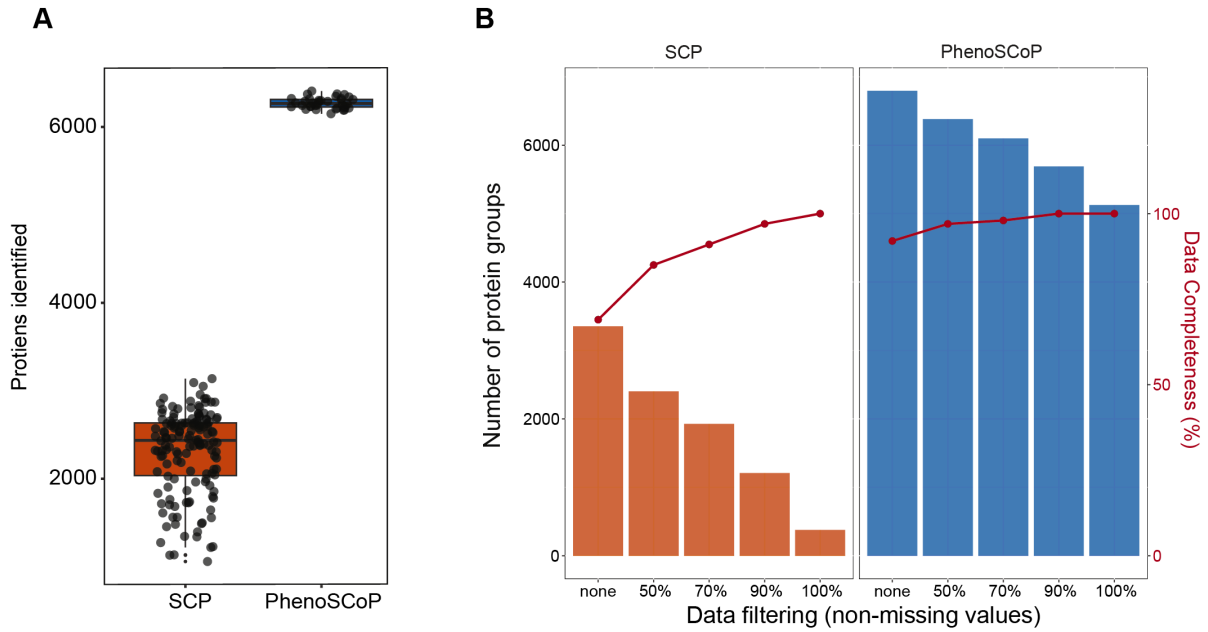

Fig. S2, related to Fig. 2. (A) Boxplot showing the number of proteins quantified using single-cell proteomics (SCP; n = 147) and PhenoSCoP (n = 36). **(B)** Comparison of protein group numbers and data completeness under different data-filtering criteria in SCP and PhenoSCoP. 'None' indicates no data filtering.

A

Genetic background of clones derived from FaDu cell line (modified from Niehr F, et al. Clin Cancer Res. 2018)	Mutant variants	Clone 46	Clone 5
	CDDP phenotype	sens	res
	CDH11 p.M275I		0.99
	CPXCR1 p.Y3S		0.99
	FN1 p.V1960I		0.99
	PTPRZ1 p.F1097	0.3	0.33
	TP53 c.673 G>A	0.99	0.64
	TP53 p.R248L		0.33
	TPO p.V674A		0.99
	Clone 5: chr 17 amplification (3 copies)		

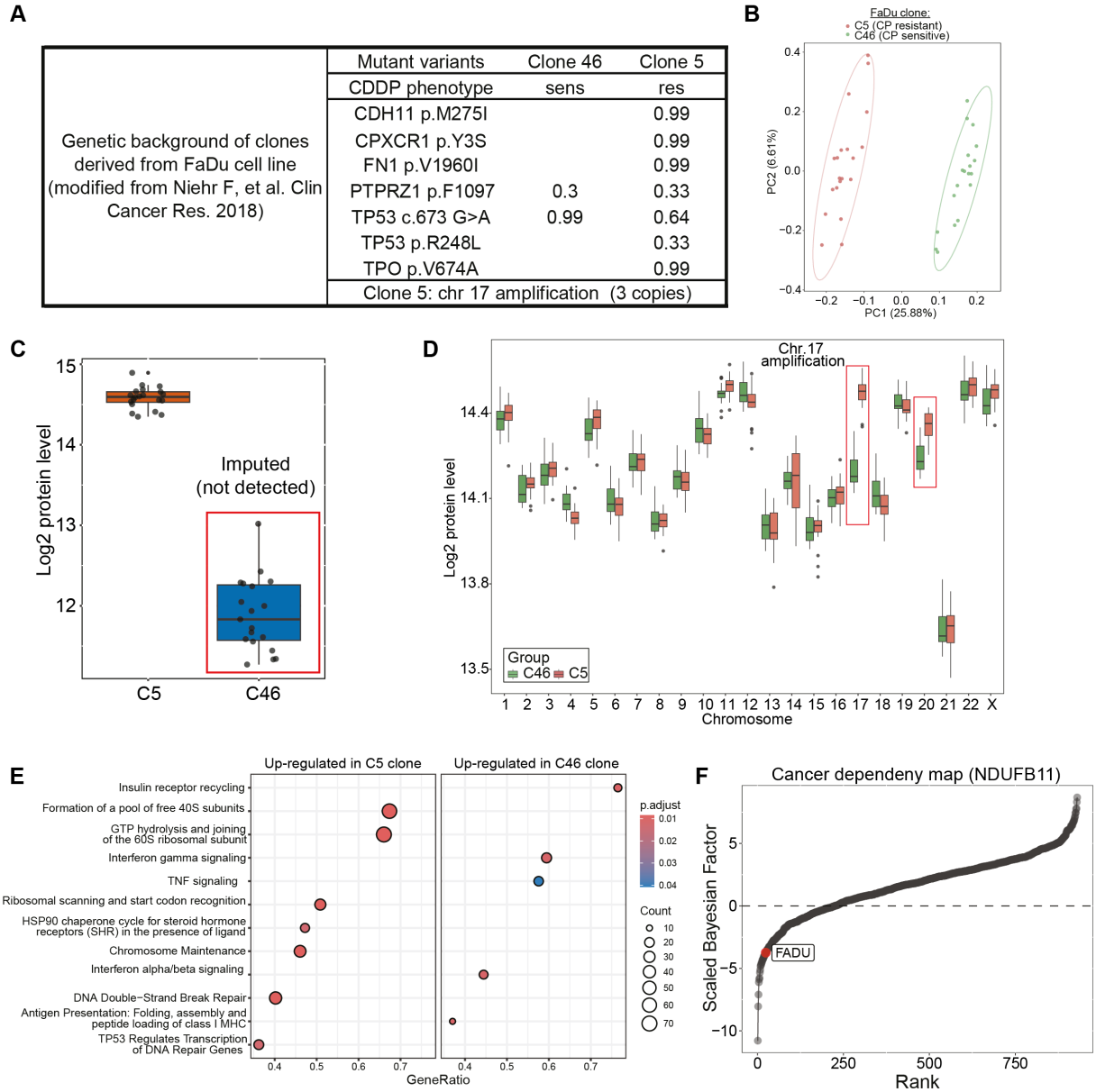

Fig. S3, related to Fig. 3. (A) Genetic background of clone-derived cell lines from FaDu. **(B)** Principal component analysis (PCA) of C5 (n = 20) and C46 (n = 19) colonies analyzed using PhenoSCoP. **(C)** Boxplot of p53 protein level (Log2) in C5 and C46 colonies. **(D)** Comparison of protein levels by chromosomal location revealed chromosome 17 and 20 specific differences. Note that C5 carried chromosome 17 amplification. **(E)** Enriched pathways (Reactome) comparing C5 and C46 colonies to identify biological differences between clones. **(F)** Dynamic plot showing the ranked scaled Bayesian factor of NDUFB11 in 930 cell models. The score of the FaDu cell line is indicated in the plot. (CRISPR: Dependencies data were downloaded from the Sanger Institute).

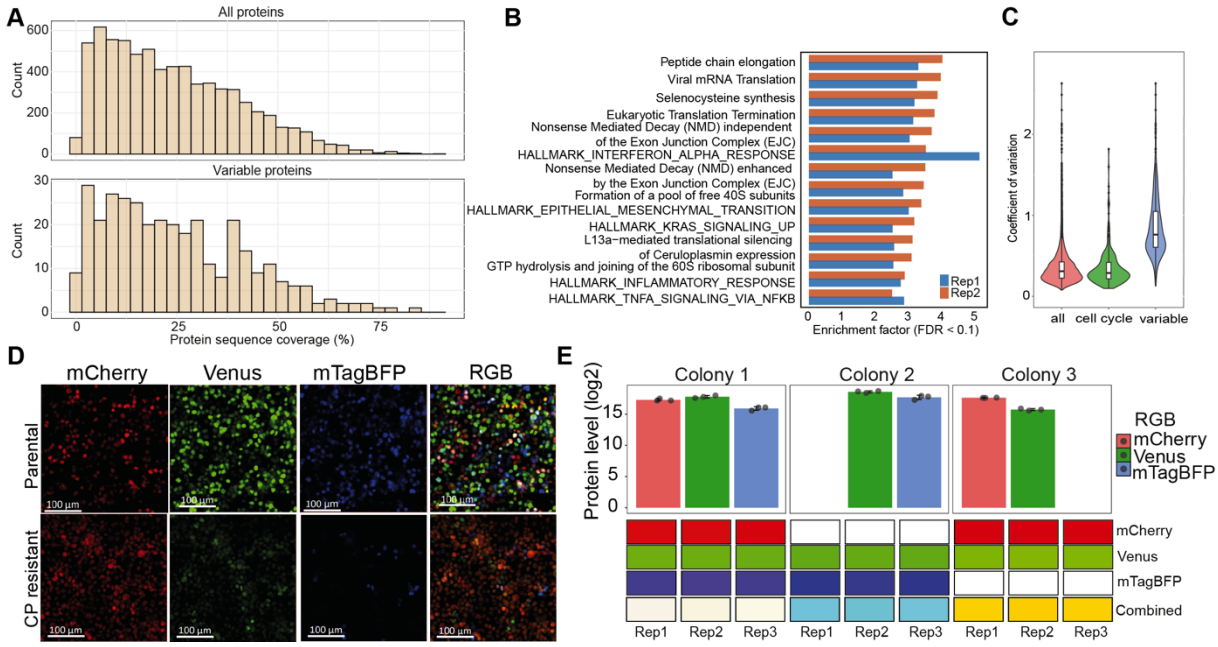

Fig. S4, related to Fig. 4. (A) Histogram of proteomic coverage for all proteins and variable proteins. **(B)** Pathway enrichment analysis of variable proteins in repeat experiments. The HALLMARK gene sets were obtained from the Human Molecular Signatures Database (MSigDB) and Reactome pathways. **(C)** Violin plots showing the distribution of the coefficient of variation (CV) for all proteins, cell cycle-related proteins (Mahdessian et al., 2021b), and variable proteins. **(D)** Representative images of RGB-labelled primary and resistant FaDu cells. Individual fluorescence channels are shown: red (mCherry), green (Venus), and blue (mTagBFP), as well as the merged RGB image. *Scale bar: 100 µm.*
(E) Quantified RGB color values for three biological replicates (each representing one-third of a colony) from each of the three colonies (n = 9 replicates in total). Upper panel: Bar plots display the mean $\log_2$-transformed protein levels corresponding to the red, green, and blue components, with error bars representing the standard deviation across replicates**.** The protein abundance for each RGB vector was normalized to a 0–255 scale across all colonies. Lower panel: RGB values for individual replicates are shown separately for each colony along with the corresponding composite virtual RGB colors generated from the quantified levels.

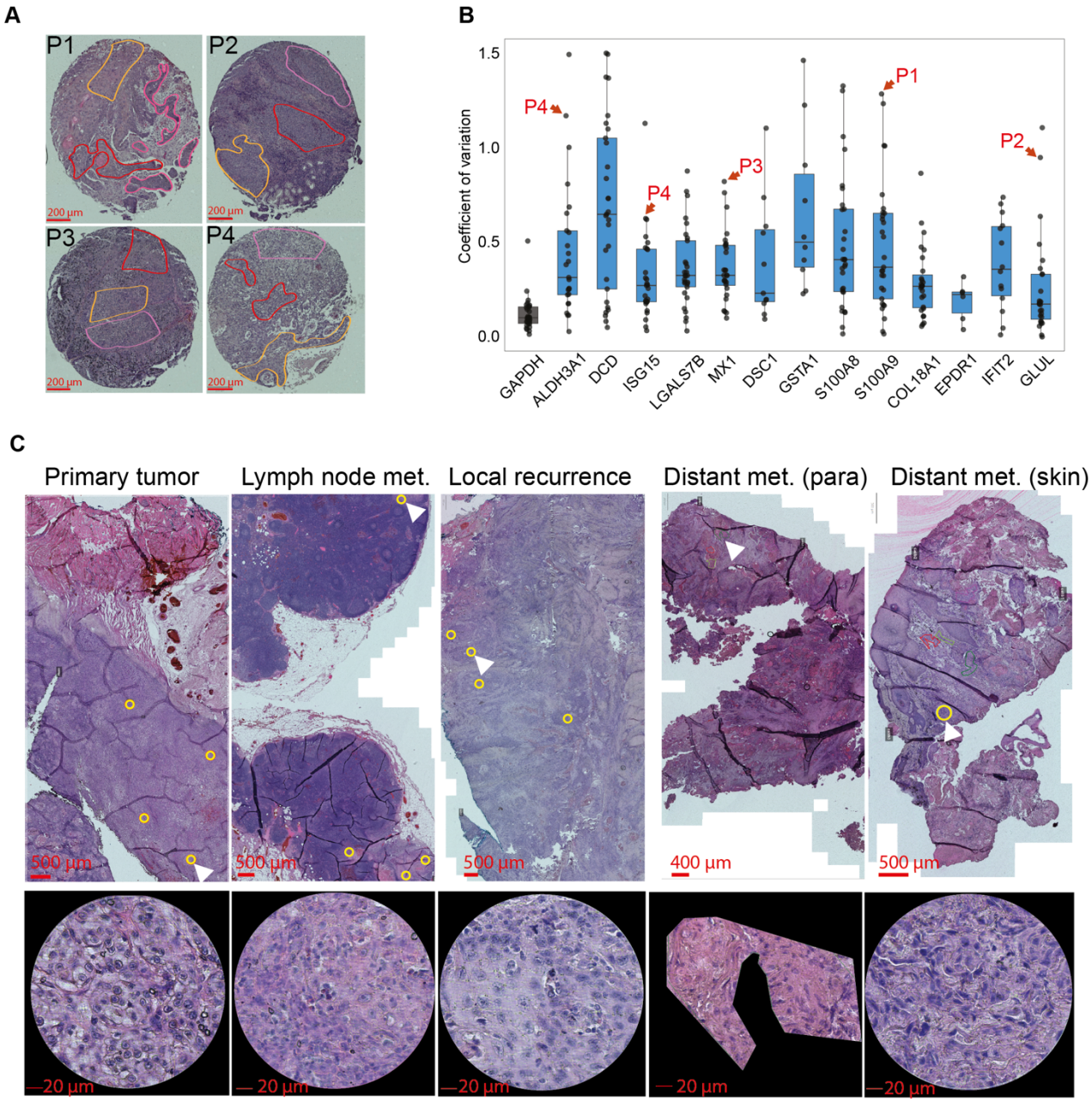

Fig. S5, related to Fig. 5. (A) Representative tissue microarray cores showing tumor regions microdissected for four patients (P1-P4). **(B)** Intra-patient heterogeneity of the most variably expressed proteins across patients. Protein CVs were calculated from three spatially distinct tumor areas per tissue section. Colors correspond to Fig. 5D. **(C)** Representative H&E images of multiple cancer tissue samples from a patient with relapse, including the primary tumor, lymph node metastasis, local recurrence, and two distant metastases (paratracheal and skin). Example regions isolated for proteomic measurements are shown in the lower panel.